②

FREE WAKE ANALYSIS OF
HELICOPTER ROTOR BLADES IN HOVER
USING A FINITE VOLUME TECHNIQUE

FINAL REPORT

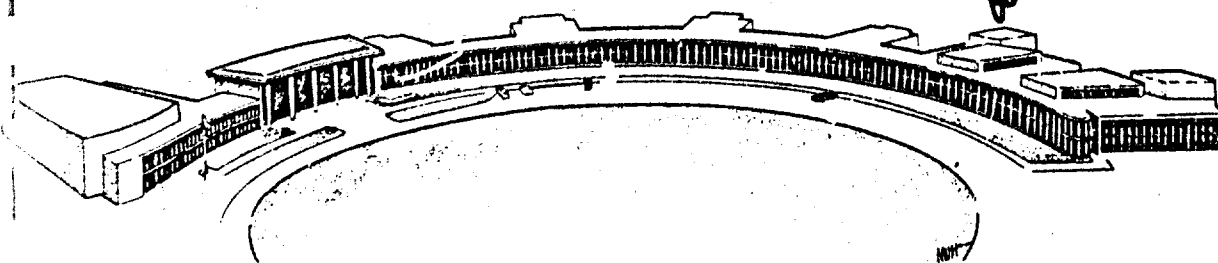### J. S. STEINHOFF AND R. KRISHNAMURTHI

OCTOBER 1988

U. S. ARMY RESEARCH OFFICE

DAAG29-84-K-0019

φH

THE UNIVERSITY of TENNESSEE
SPACE INSTITUTE

Tullahoma, Tennessee

89 1 17 299

REPORT DOCUMENTATION PAGE

1a. REPORT SECURITY CLASSIFICATION	1b. RESTRICTIVE MARKINGS
Unclassified	

2a. SECURITY CLASSIFICATION AUTHORITY	3. DISTRIBUTION / AVAILABILITY OF REPORT
2b. DECLASSIFICATION / DOWNGRADING SCHEDULE	Approved for public release; distribution unlimited.

4. PERFORMING ORGANIZATION REPORT NUMBER(S)	5. MONITORING ORGANIZATION REPORT NUMBER(S)
	ARO 20895.5-EG

6a. NAME OF PERFORMING ORGANIZATION	6b. OFFICE SYMBOL (If applicable)	7a. NAME OF MONITORING ORGANIZATION
The University of Tennessee Space Institute	N/A	U. S. Army Research Office

6c. ADDRESS (City, State, and ZIP Code)	7b. ADDRESS (City, State, and ZIP Code)
Engineering Science Department Upper E Tullahoma, TN 37388	P. O. Box 12211 Research Triangle Park, NC 27709-2211

8a. NAME OF FUNDING / SPONSORING ORGANIZATION	8b. OFFICE SYMBOL (If applicable)	9. PROCUREMENT INSTRUMENT IDENTIFICATION NUMBER
U. S. Army Research Office		DAAG29-84-K-0019

8c. ADDRESS (City, State, and ZIP Code)	10. SOURCE OF FUNDING NUMBERS			
P. O. Box 12211 Research Triangle Park, NC 27709-2211	PROGRAM ELEMENT NO.	PROJECT NO.	TASK NO.	WORK UNIT ACCESSION NO.

11. TITLE (Include Security Classification)

Free Wake Analysis of Helicopter Rotor Blades in Hover Using a Finite Volume Technique

12. PERSONAL AUTHOR(S)

J. S. Steinhoff and R. Krishnamurthi

13a. TYPE OF REPORT	13b. TIME COVERED	14. DATE OF REPORT (Year, Month, Day)	15. PAGE COUNT
Final	FROM 2/1/84 TO 7/31/88	88,10,28	96

16. SUPPLEMENTARY NOTATION The view, opinions and/or findings contained in this report are those of the author(s) and should not be construed as an official Department of the Army position, policy, or decision, unless so designated by other documentation.

17.	COSATI CODES		18. SUBJECT TERMS (Continue on reverse if necessary and identify by block number)
FIELD	GROUP	SUB-GROUP	Computational Fluid Dynamics, Vortex, Helicopter Roter

19. ABSTRACT (Continue on reverse if necessary and identify by block number)

In the computation of helicopter rotor flow fields, wake effects can be very important since each blade passes close to the wake produced by the preceding ones, causing a large local effect. Also, the vortical flow from the wake of a number of blade passages causes a large global effect. Extensive work has been done on helicopter rotor flows using integral methods to follow the vortex wake. These generally cannot treat compressibility effects. Also, they have difficulty attaining stable solutions, particularly in hover, where a large number of interacting vortex sheets must be treated.

A new method has been developed which like integral methods does not constrain or spread the wake. Also, like finite difference methods, it can treat compressibility effects. This method has been developed into a computer program for the computation of rotor flow fields in hover with free wakes. The method utilizes a finite volume potential flow technique. The basic approach involves modifying the potential flow wake treatment so that, within the numerical approximation, the momentum is conserved there as in the rest of the flow field. The internal structure of the vortex is not solved for, but is modeled and spread over several grid points. The wake position and vorticity strength are computed so that the momentum over the wake is balanced in an integral sense. Results computed by this approach for the circulation and wake geometry are compared with experimentally measured data. Cases treated include subsonic and transonic flows, high and low aspect ratios, and two and four-bladed rotor configurations. (SDW)

20. DISTRIBUTION / AVAILABILITY OF ABSTRACT	21. ABSTRACT SECURITY CLASSIFICATION
☐ UNCLASSIFIED/UNLIMITED ☐ SAME AS RPT. ☐ DTIC USERS	Unclassified

22a. NAME OF RESPONSIBLE INDIVIDUAL	22b. TELEPHONE (Include Area Code)	22c. OFFICE SYMBOL

DD FORM 1473, 84 MAR

83 APR edition may be used until exhausted.
All other editions are obsolete.

FREE WAKE ANALYSIS OF HELICOPTER ROTOR BLADES IN HOVER USING A FINITE VOLUME TECHNIQUE

FINAL REPORT

J. S. STEINHOFF AND R. KRISHNAMURTHI

OCTOBER 1988

ACKNOWLEDGEMENTS

QUALITY
INSPECTED
1

Accession For	
NTIS GRA&I	☑
DTIC TAB	☐
Unannounced	☐
Justification	

By_____
Distribution/
Availability Codes

Dist	Avail and/or Special
A-1	

ABSTRACT

In the computation of helicopter rotor flow fields, wake effects can be very important since each blade passes close to the wake produced by the preceding ones, causing a large local effect. Also, the vortical flow from the wake of a number of blade passages causes a large global effect. Extensive work has been done on helicopter rotor flows using integral methods to follow the vortex wake. These generally cannot treat compressibility effects. Also, they have difficulty attaining stable solutions, particularly in hover, where a large number of interacting vortex sheets must be treated.

A new method has been developed which like integral methods does not constrain or spread the wake. Also, like finite difference methods, it can treat compressibility effects. This method has been developed into a computer program for the computation of rotor flow fields in hover with free wakes. The method utilizes a finite volume potential flow technique. The basic approach involves modifying the potential flow wake treatment so that, within the numerical approximation, the momentum is conserved there as in the rest of the flow field. The internal structure of the vortex is not solved for, but is modeled and spread over several grid points. The wake position and vorticity strength are computed so that the momentum over the wake is balanced in an integral sense. Results computed by this approach for the circulation and wake geometry are compared with experimentally measured data. Cases treated include subsonic and transonic flows, high and low aspect ratios, and two and four-bladed rotor configurations.

TABLE OF CONTENTS

LIST OF FIGURES

LIST OF SYMBOLS AND ABBREVIATIONS

A	rotor disk area, πR^2
AR	blade aspect ratio, rotor radius divided by chord
b	number of blades
c	blade chord
C_ℓ	section lift coefficient
c_p	pressure coefficient
C	normalization constant for vortical velocity
C_T	rotor thrust coefficient, $\frac{T}{\rho \pi R^2 (\Omega R)^2}$
h	transformation Jacobian
k_1	average axial velocity of a tip vortex from the time it was shed by a given blade until it passes the following blade, normalized by tip speed, ΩR
k_2	average axial velocity of a tip vortex generated by a given blade after it passes the following blade, normalized by tip speed, ΩR
M	local blade Mach number
M_T	Mach number of blade tip
P	representative point at which velocity is calculated
$\vec{q}$	local total velocity
$\vec{q}^{\,v}$	local vortical velocity
R	rotor radius
r	local radius of the span station
T	rotor thrust

u	physical velocity in x-direction
U	contravariant velocity normal to YZ plane
V	contravariant velocity normal to ZX plane
v	physical velocity in y-direction
w	physical velocity in z-direction
W	contravariant velocity normal to XY plane
Γ	bound circulation
γ	ratio of specific heats, $\gamma = 1.4$ for all calculations
ρ	air density
σ'	rotor solidity, ratio of total blade area to disc area, $\frac{bc}{\pi R}$
ψ	vortex azimuth angle
Ω	rotor angular velocity
θ	blade azimuth angle
ϕ	velocity potential
ω	vorticity

Mathematical Expressions

Im	Imaginary component of complex function

CHAPTER 1

INTRODUCTION

The task of predicting the flow field and airloads of a helicopter rotor continues to be of primary importance for providing and evaluating improved rotor designs. Unfortunately, rotary-wing flow fields are among the most complex in aerodynamics. Recently, application of higher level computational aerodynamics techniques to this problem has become possible with the advent of high speed large memory computers. Computational studies have been conducted to investigate the influence of the rotor wake and develop methodology for predicting the rotor flow field and blade airloads [1]. Most current methods for computing rotor flow fields, including wakes, are based on integral or finite difference techniques [2]. Integral methods, in the form of lifting line or lifting surface methods, are able to treat the rotor blades as well as the wake in a single unified way [3]. They, however, have several disadvantages: they are restricted to linear, low speed incompressible cases and they have difficulty attaining stable solutions in hover where a large number of interacting vortex sheets must be treated. Finite difference methods (also finite volume and finite element), on the other hand, usually can treat compressibilty effects and can accurately solve for flow in the immediate region of the blade. Most of these methods, which include Potential Flow and Euler based methods, however, do not treat the flow field in a single unified way: they isolate the region close to the blade and only solve the difference equations in those regions. The entire vortex system is currently treated in these methods by coupling with an integral technique, such as a classical lifting line or lifting surface method. This vortex calculation is used to determine an induced velocity on the surface of the finite difference grid surrounding each blade, which is then used as a boundary

condition for the finite difference calculation in a coupled iteration scheme.

1.1 Background

For hovering rotor wake geometry, the fundamental wake structure was confirmed in the 1960's and early 1970's during model rotor tests of rotors with varying numbers of blades, twist, taper, camber, tip shape, thrust level, and tip speed [4]. Smoke flow visualization was used to photograph cross sections of the wake as shown in the sample flow visualization photograph in Figure 1. The fundamental wake contains two primary components. The first, and most prominent, is the strong tip vortex which arises from the rapid rolling up of the portion of the vortex sheet shed from the tip region of the blade. The second feature is the vortex sheet shed from the inboard portion of the blade (Figure 2). Flow visualization photographic data were analyzed to determine wake coordinates for various rotor designs and operating conditions. Generalized wake equations were developed for the tip vortex and inboard wake geometry, as generalized functions of number of blades, twist, and thrust level [4, 5]. The characteristics of the wake geometry largely result from the velocities induced by the strong tip vortex. The exact nature of this, however, has been difficult to distinguish in flow visualization studies.

1.2 Rotor Analysis in Hover

An understanding of rotor wake behavior is of primary importance in the prediction of aerodymamic loading. It is clear that any complete analysis of the rotor problem must account for four distinct yet coupled phenomena:
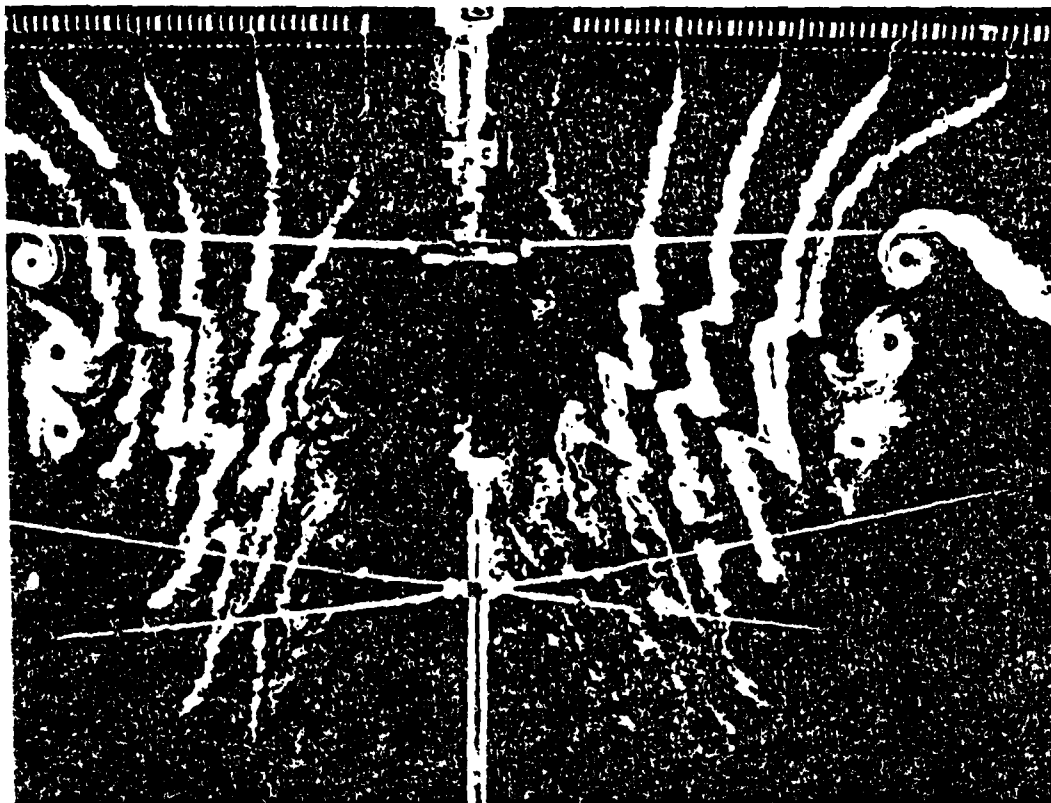
Figure 1: Sample Flow Visualization Photograph (From Reference [4])
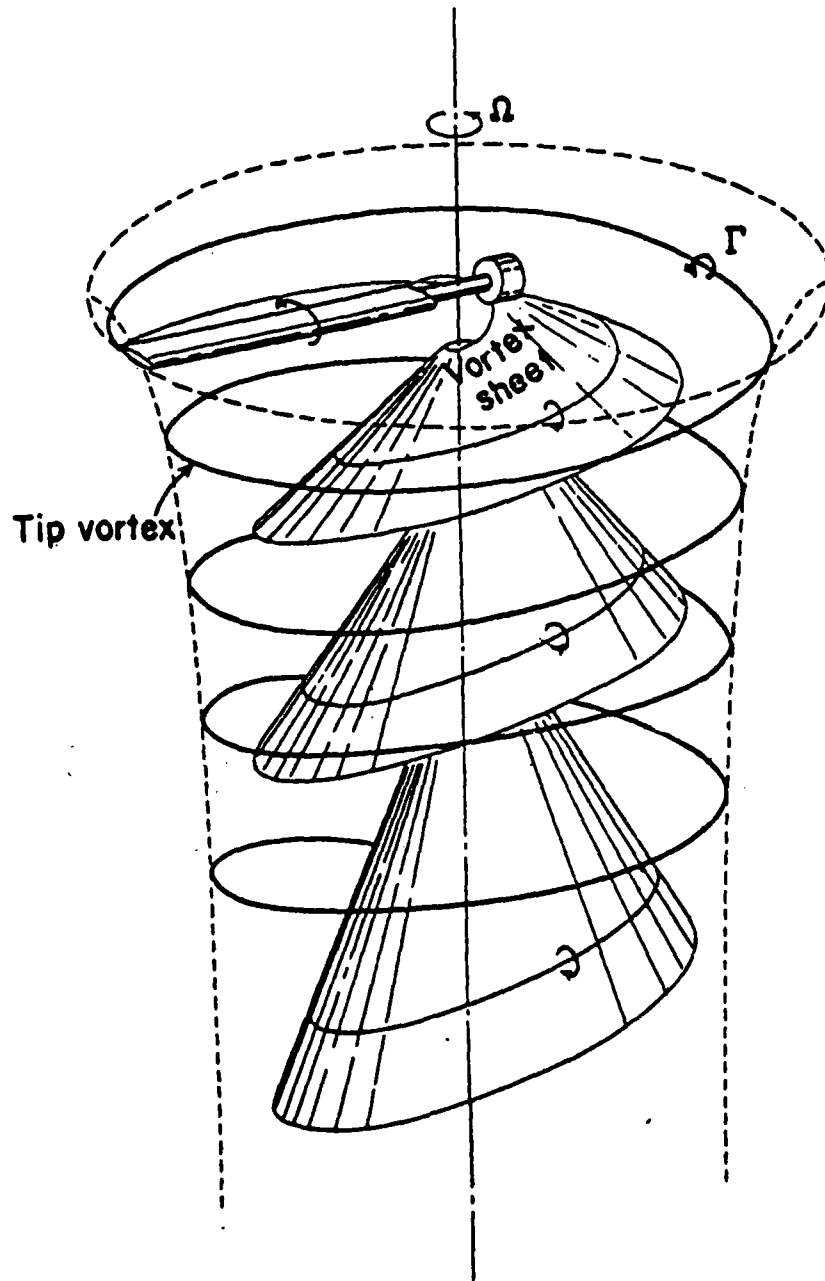
Figure 2: Schematic of Rotor Wake Structure (From Reference [4])

1) the nonlinear compressible flow near the blade;

2) the highly complex vortex structure;

3) close blade-vortex interactions;

4) viscous flow phenomena such as stall.

Analyses for each of these aspects of the problem already exist, though not in a rigorously coupled form. A major question in advanced aerodynamic methods is how can the wake be included in rotor flow field analysis. A number of approaches for modeling the wake have been developed. In the wake modeling approach, the analysis can be resolved into three components: the aerodynamic theory used for the inflow solution, the method of calculating rotor performance from the inflow solution, and the wake model.

By far the most common flow analysis methods currently used in the rotor industry are various integral formulations of the potential equation. These include panel methods, lifting line and lifting surface approaches. This class of schemes provides the easiest and most efficient methods to predict the inflow induced by the rotor's complex wake system when the geometry of the system can be specified á priori. The analysis based on a lifting line representation for the blade is reported to predict hover performance for a wide range of rotors [6]. But this representation is not suitable for complex planforms. Lifting surface methods have been applied to hovering rotor analysis by a number of investigators [7, 8]. Typically, modeling of the influence of the complete rotor and wake has been accomplished with these methods. In this approach the blade geometry is represented by a thin surface composed of a number of conveniently chosen trapezoidal panels, forming a vortex circuit in the form of a rectangle. The geometry of the wake is either computed or prescribed. The wake is also represented by a multiple vortex circuit system.

Most of the effects of compressibility cannot be obtained by this method.

Panel methods use a surface singularity distribution to solve the linear potential equation for arbitrary geometry [9] . The use of a velocity potential reduces the problem to the solution of an integral equation for a scalar function. A free wake analysis, which is the most sophisticated approach to wake modeling, considers the wake as a free vortex flow. A number of the panel method solutions for the hovering rotor include a free wake geometry calculation [10,11,12]. In these, the wake is divided into near, intermediate, and far wake regions. Vortex filaments are distributed in the near and intermediate wake regions and an analytical model used to represent the far-wake.

Miller [11] developed a hover free wake geometry calculation, using two-dimensional and axisymmetric models for efficiency. The wake was assumed to have rolled up into three vortices (tip, inboard, and root) which were replaced by a far wake model after four revolutions. Murman and Stremel [12] calculated two-dimensional unsteady wake development by a cloud-in-cell method. Discrete vortex elements in the wake were tracked in a Lagrangian frame. For each time step, the vorticity was distributed to a fixed mesh, on which the velocities were calculated by a finite difference solution of Laplace's equation. Stremel [13] applied this two-dimensional model to hovering rotor wake roll-up. Roberts [14] developed a cloud-in-cell method to calculate hovering rotor wake geometry.

In recent years a number of finite-difference codes for the prediction of transonic rotor flows has been developed. Egolf and Sparks [15] coupled a full potential solution for the near field of a hovering rotor blade with an incompressible discrete vortex solution for the far field. The wake geometry was prescribed, and the far

field solution determined the velocity potential on the boundaries of a finite differ-ence computational domain. Sankar et al [16] solved three dimensional unsteady Euler equations for a hovering rotor in a small box around each blade. Caradonna and Strawn [17] solved the full potential equation in conservative form also in a box around each blade and incorporated a wake modeling scheme. The basic ap-proach to this wake modeling was to separate the rotor wake system into two parts. The most important part, the tip vortices, were explicitly modeled in the finite difference solution procedure when they were inside the computational box. The second part of the wake system, consisting of vorticity elements that were outside the computational grid, was modeled with an inflow boundary condition at the boundary of the computational grid. A similar method was developed by Tung and Chang [18] with a non-conservative formulation of the potential equation.

The approach used in these finite-difference methods to include the total wake influence has been to include the effects of near vortices in the form of an inflow boundary condition applied on the surface [17] with the inflow being determined by a Biot-Savart computation. The outer vorticity contributions are included either on the grid outer boundary or specified as a spanwise varying correction to the blade twist distribution.

The investigation presented herein describes a unified method that is fully compressible and which computes the wake without requiring external specification of the wake, or separate computations for the wake and blade region. The problems associated with other methods are avoided by using an embedding procedure by which vorticity layers can be put anywhere in the grid. The method is based on the fact that any flow field can be decomposed into potential and vortical parts. A potential is defined on a set of grid points, as in standard potential

methods. Also, as in these methods, mass balance relations are enforced at each point on the grid. The potential, however, does not have any discontinuities, and therefore does not represent any vorticity. The vorticity is represented by a separate velocity field which is added to the gradient of the potential. The location and strength of this velocity field is determined by momentum considerations. This added field is concentrated in sheets, as is the vorticity that results from it. No external specification of the strength of these sheets or their location is required: momentum conservation relations together with mass balance relations are used to determine these. This is believed to be the first complete treatment of this problem. The method utilizes a modification of a compressible finite volume potential flow technique frequently used in fixed-wing analysis, which has been developed into a computer program for the computation of compressible rotor flow fields in hover with free wakes. Free wake geometry determined with this new wake treatment are in substantial agreement with experiment.

CHAPTER 2

GENERAL ANALYSIS

2.1 Elementary Considerations of Hovering Rotor

In the momentum theory analysis the rotor is modeled as an actuator disk, which is a circular surface of zero thickness that can support a pressure difference. The flow problem is solved by using the basic conservation laws of fluid motion. The actuator disk model is only an approximation to the actual rotor. Momentum theory gives the induced power per unit thrust for a hovering rotor:

$$v_{induced} = P/T = \sqrt{\frac{T}{2\rho A}}$$

This relation determines the basic characteristic of helicopter rotor. Simple momentum theory provides some understanding of the basic relationships between such important design parameters as disc loading and power required per unit of thrust. However, this theory has serious limitations in providing guidance for rotor design and does not provide a physical concept that could explain the nonuniformities of downwash velocities.

Vortex theory uses the Biot-Savart law for the velocity induced by the wake vorticity. In this approach the rotor is modeled by segments of a vortex filament. The vortex elements are allowed to be transported by the resultant velocity of the free stream and vortex induced velocities calculated using the Biot-Savart law. The computational procedure required in the free wake analysis is huge and can be accomplished only by the use of high capacity computers. In addition, various safeguards must be used to avoid mathematical singularities that have no physical counterpart.

In recent years a substantial number of finite-difference codes for the prediction of three-dimensional transonic flows have been developed. These codes have been successfully used in fixed-wing flow analysis. The development and use of corresponding rotary-wing codes has proceeded very slowly. A primary reason for this delay is the much greater complexity of the rotor environment.

Classical lifting-line theory treats the case of a high aspect-ratio, planar, fixed wing in steady flow. In the linearized model both the wing and wake are represented by this planar sheet of vorticity. For the fixed wing the distortion of the wake and the rollup of tip vortices can generally be neglected, because the wake is convected downstream away from the wing. The basic assumption of lifting-line theory, that the wing has high aspect ratio, can sometimes be satisfied with a rotor blade. However, the requirement that there be no rapid change in spanwise circulation restricts the validity of lifting-line theory rotor flow even though the geometric aspect ratio is large. There are two important regions of general rotor flow fields where this requirement is not satisfied: at the blade tip and near a blade-vortex interaction. On rotor blades the loading is typically concentrated near the tip because of the rotation of the blade, and the gradient of the lift is particularly high there. Hence, any small distortion of the loading due to the three dimensional flow effect is very important. Conservation of vorticity requires that the bound circulation be trailed into the wake from the blade tip and root. The vorticity is also left in the rotor wake as a consequence of radial and azimuthal change in the bound circulation (Figure 3). In classical theory, the trailing vorticity, γ_t, which is due to the radial variation in bound circulation, is parallel to the free stream. The shed vorticity, γ_s, due to the azimuthal variation in bound circulation, is oriented radially in the wake. The strength of the rotor trailing and
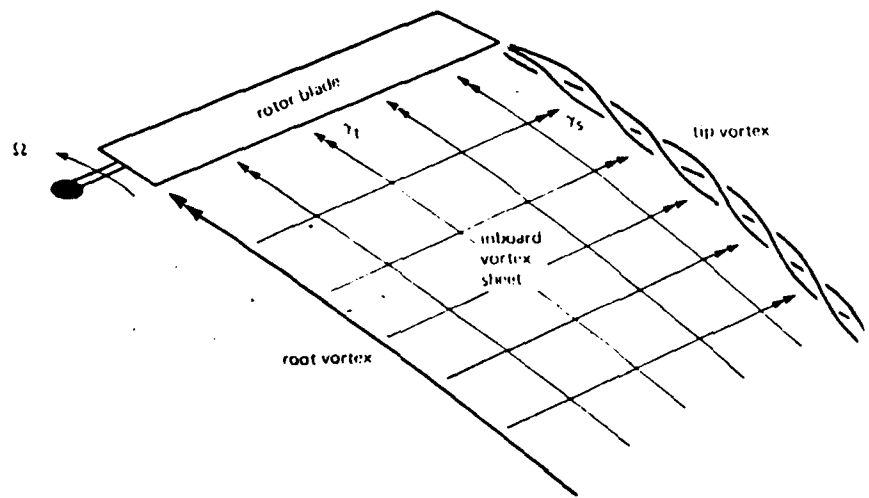
Figure 3: Schematic of Trailed and Shed Vorticity in Rotor Wake (From
Reference [19])

shed vorticity are given by,

$$\gamma_t = \frac{\partial \Gamma}{\partial r}$$

$$\gamma_s = -\frac{1}{U_T}\frac{\partial \Gamma}{\partial t}$$

Hover is the operating state in which the lifting rotor has no forward velocity relative to the air. This implies axial symmetry of the rotor, and hence, that loads on the rotor blades are independent of the azimuth position. Hence, this particular shed vorticity is not of importance in hover airload computations. While the circulation drops to zero over a finite distance, the rate of decrease is still very high. The result is a large trailing vorticity strength at the outer edge of the wake, causing the vortex sheet to roll up into a concentrated tip vortex. The tip vortex has a small core radius that depends on the blade geometry and loading. On the inboard portion of the blade, the bound circulation drops off gradually to zero at the root. Hence there is an inboard sheet of trailed vorticity in the wake with opposite sign to the tip vortex. Since the gradient of the bound circulation is low, the root vortex is generally much weaker and more diffused than the tip vortex. Hence, the strong concentrated tip vortices are by far the dominant feature of the rotor wake. In addition, because of its rotation, a rotor blade encounters the tip vortex from the preceding blade. When a vortex passes close to the blade it induces a large velocity and hence a large change in loading on the rotor. Methods have been developed to calculate the nonuniform inflow due to the wake, the self induced distortion of the wake, and the vortex induced loads [19]. From the dominant role of the tip vortices in determining the inflow and loading, it follows that the determination of its position is the most important part of the rotor wake geometry calculation.

2.2 Hovering Rotor Wake Models

There are a number of methods used to specify wake geometry in rotary wing analysis. The rigid wake model implies an undisturbed helical geometry, in which all the wake elements are convected with the same mean axial velocity. In this model, the wake consists of helical vortex sheets that move as rigid surfaces with uniform velocity and no distortion. The transport velocity of the wake is determined by rotor disk loading, and the pitch of the helical surface is determined by the axial and rotational velocity of the blades. The wake movement imparts a velocity to the fluid at the wake surface. In the limit of an infinite number of blades, the sheets are very close and as a consequence all the fluid is carried with the wake and there are no losses due to flow around the edges. With a finite number of blades there will be radial flow as well, which decreases the lift at the blade tip. An elementary extension of this model is the semi-rigid wake model, in which each element is convected downward with the induced velocity at the point on the rotor where it was created. The simplest wake model including the effects of a finite number of blades consists of helical vortex sheets trailed from each blade. The major effect of the finite number of blades is a reduction of the loading at the blade tip. This effect is generally represented by a tip loss correction for a finite number of blades.

A wake model consisting of undistorted vortex sheets is not adequate for helicopter rotors, where the interference between the rotor blade and wake vorticity, and the self induced distortion in the wake, are important. The trailed vorticity quickly rolls up into concentrated tip vortices that remain close to the rotor and strongly influence the loading near the tips of both generating and following blades. The most accurate specification of the wake is the free wake model. This

includes the distortion from the basic helix, as each wake element is convected with the local flow, including the velocity induced by the wake itself. When measured wake geometry information is used, instead of a calculation this is called a prescribed wake model. Clark and Leiper [20] developed a method for calculating the distorted wake geometry of hovering rotors. Their wake model consisted of a number of constant strength trailed-vortex lines. The far wake was approximated by segments of ring vortices. Two revolutions of the free wake were used, followed by 30 revolutions of far wake. Landgrebe [4] conducted an experimental investigation of the performance and wake geometry of a model hovering rotor. The wake geometry was measured by flow visualization, and the data was used to develop expressions for the axial convection and radial contraction of the tip vortices. The tip vortex elements were found to have a roughly constant descent rate before and after passing beneath the following blade. Prior to the encounter with the blade the descent rate is approximately proportional to the blade loading, C_T/σ. After the encounter the axial convection rate is higher and is approximately proportional to the mean inflow, $\sqrt{C_T/2}$. This generalized wake geometry information was used in rotor performance calculations. Scully [21] developed a free wake analysis method for a helicopter rotor. The procedure for calculating wake geometry consisted basically of integrating the induced velocity at each wake element. Once the wake geometry is specified, either a lifting surface or a lifting-line theory can be used to obtain blade loading.

2.3 Potential Flow Methods

Lifting surface theory retains the mutual interaction of all elements of the rotor and wake by representing the rotary-wing by vortex surfaces and by satisfying appropriate boundary conditions over the entire surface. A free wake geometry

calculation is required, and also a calculation of the tip vortex roll-up and other fine structures of the wake. Hence, the computation time required increases rapidly with the number of elements used to represent the blade/vortex system.

From the above discussion of these vortex theories, it can be seen that, though they offer a precise description of the rotor aerodynamics in practical application, they require a large amount of computational effort. The application of a velocity potential which will be described below, makes it possible to determine steady and unsteady flow fields induced by the rotor in both incompressible and compressible fluids with a precision similar to that offered by the above vortex theories but with less computational effort.

2.3.1 Velocity Potential in Incompressible Flow

The continuity equation for an incompressible fluid requires that

$$\frac{\partial u}{\partial x} + \frac{\partial v}{\partial y} + \frac{\partial w}{\partial z} = 0$$

further restricting this perfect fluid to be irrotational leads to the existence of a velocity potential, ϕ. The components of the velocity vector associated with ϕ can be obtained as

$$\vec{v}(P) = \cdot\vec{\nabla}\phi(P)$$

The condition of continuity can then be written as

$$\vec{\nabla}\cdot\vec{\nabla}\phi \equiv \frac{\partial^2\phi}{\partial x^2} + \frac{\partial^2\phi}{\partial y^2} + \frac{\partial^2\phi}{\partial z^2} = 0$$

resulting in Laplace's equation for ϕ.

Solution to this can be expressed as

$$\phi(x_,,y_,,z_,) = \int\int\left[\phi\frac{\partial}{\partial r}\left(\frac{1}{4\pi r}\right) - \frac{1}{4\pi}\frac{\partial\phi}{\partial r}\right]dB$$

This equation relates the potential at an arbitrary point in the fluid to the superposition of potentials due to doublet and source singularities distributed on the body surface. Kocurek [21] applied this singularity type of discretization to solve the problem of a hovering rotor.

2.3.2 Potential Methods in Compressible Fluids

At present a number of schemes are being developed to compute compressible flows. A variety of approaches use potential methods. The transonic flow past a non-lifting, hovering rectangular rotor was first solved by Caradonna and Isom [22]. They developed a finite difference calculation procedure for the Transonic Small Disturbance equation. Later, it was extended to solve the Full Potential equation. For lifting rotors, the conventional potential flow method was not able to treat the rotor blade as well as the wake in a single unified way. In this method, the vortex sheets are treated as discontinuities in the potential, which constrains the sheets to lie on segments of surfaces of the computational grid. Accordingly, in conventional potential methods, only short segments of the sheet, which are fairly flat, and where the grid can be distorted to follow the sheet, can be accurately treated.

More recently, a coupled iteration scheme has been developed where a finite difference solution procedure is obtained in a small region near each blade. The computation in this grid is coupled to an exterior vortex filament wake model, which describes almost all of the wake influence. Unfortunately there are major drawbacks to this approach. First, unlike the computation, there is no clear separation in the physical flow between the wake and the flow in the blade region. If accurate solutions are to be obtained, the flow region that is computed using the

compressible method on the grid must extend a large number of chords from the blade. The wake then typically penetrates this region and must be treated within the grid. Since the size of this region as well as the wake geometry near the blade will depend sensitively on the flow conditions, deciding which portion of the wake spirals must be included in the grid can be complicated for the general cases. Further, simply embedding the vortex sheet as a potential discontinuity or embedded line vortices is only feasible for simple cases, such as where the sheet rolls up into a single well-defined vortex near the tip and one near the root. Further drawbacks concern the feasibility of treating the general wake, even outside of the grid region, as a collection of vortex filaments. While this is possible in simple cases, in general it is very difficult since the vortical regions can leave the blade with even the signs of vorticity varying along the blade. Also if there are a large number of filaments, these must be integrated over each time step to determine the velocity induced by the wake over the outer boundaries of the grid regions. Accurately interfacing this calculation with a set of grids near each blade would appear to be complicated. Furthermore, a filament approach complicates the computation of near blade-vortex interactions because special smoothing must be applied near each filament to eliminate locally infinite velocities.

2.3.3 Vortex Embedding Method

The basic approach described herein involves modifying the potential flow wake treatment so that, within the numerical approximation, momentum is conserved there, as in the rest of the field. The internal structure of the vortex sheet is not solved for, but is modeled and spread over several grid points. The wake position and vorticity strength are computed so that momentum over the wake is balanced in an integral sense. The potential is defined on a set of grid points as in

standard methods. Also, as in these methods, mass balance relations are enforced at each point on the grid. However, the potential does not have any discontinuities, and therefore does not represent any vorticity. The vorticity is represented by a separate velocity field which is added to the gradient of the potential. This added field is concentrated in sheets, as is the vorticity that results from it. No external specification of the strength of these sheets or their locations is required: momentum conservation relations are used to determine these, together with the mass balance relation. Thus, it is a true free-wake method.

Initial use of the method for a vortex line convecting past a wing in compressible flow was published in 1983 [22]. A preliminary use of the method for roll-up of vortex sheets was also published in 1983 [23].

2.3.4 Description of the Vortex Embedding Procedure

The basis of the Vortex Embedding procedure lies in the fact that any velocity $\vec{q}$ can be expressed as the sum of potential and vortical components. First the velocity is decomposed into a free stream, potential, and vortical part:

$$\vec{q} = \begin{pmatrix} u \\ v \\ w \end{pmatrix} = \vec{\omega} \times \vec{r} + \vec{\nabla}\phi + \vec{q}^{\,v} \tag{1}$$

where $\vec{\omega}$ is the rotor angular velocity, directed along the axis, $\vec{r}$ is normal to the axis and

$$\vec{\omega} = \nabla \times \vec{q}^{\,v}.$$

The vortical part, $\vec{q}^{\,v}$, is concentrated near the sheet. This decomposition is made especially powerful by the fact that for a given $\vec{\omega}$ distribution $\vec{q}^{\,v}$ is not unique. This can produce some very useful simplifications in various flow models. For instance, in a typical potential computation for the lifting flow about a wing, the

entire velocity is usually represented by the potential, ϕ (that is $\vec{q}^{\,v} = 0$). However, the production of lift implies the shedding of vorticity. With a potential alone this can only be represented by a sheet along which ϕ is discontinuous and where the magnitude of this discontinuity is Γ, the shed circulation. This sheet typically must lie along a grid coordinate. However, the use of velocity decomposition allows a considerable simplification and versatility in the sheet description. The basic idea is to spread the sheet into a thin vorticity region described by an appropriate velocity distribution, $\vec{q}^{\,v}$.

A fixed grid (in the rotating blade-fixed frame) is used to solve the compressible-potential equation for the potential, ϕ:

$$\partial_x(\rho u) + \partial_y(\rho v) + \partial_z(\rho w) = 0 \qquad (2)$$

where ρ is the density and has the isentropic form away from the sheet based on the total velocity, $\vec{q}$, with components u, v and w.

$$\rho = \left[1 - (\frac{\gamma-1}{2})M_\infty^2((\vec{\omega} \times \vec{r})^2 - \vec{q}^{\,2})\right]^{\frac{1}{\gamma-1}} \qquad (3)$$

The vortical component, $\vec{q}^{\,v}$, is spread over several grid points around the vortex sheet so that the vorticity is concentrated there. $\vec{q}^{\,v}$ satisfies

$$\vec{\nabla} \times \vec{q}^{\,v} = \vec{\omega}$$

During the iteration towards convergence (the solution is steady in the blade coordinate system for hover) a four step procedure is used repeatedly:

1. The vortex position is integrated as a set of marker streamlines to follow the flow using interpolated value of $\vec{q}$ from fixed grid;

2. $\vec{q}^{\,\nu}$ is computed at grid points near the sheet;

3. A potential, ϕ is computed at each grid point to satisfy Equation (2) with $\vec{q}^{\,\nu}$ fixed.

4. A new velocity $\vec{q}$ is computed at each grid point based on Equation (1).

At convergence Equation (2) is satisfied and the vortex sheet follows the flow. Although the vortex sheet is effectively spread over several grid points, $\vec{q}^{\,\nu}$ is a continuous vortical velocity field which suffers no artificial numerical diffusion. The internal structure of the sheet can be modeled by simply choosing appropriate values or solved for using a viscous flow solution. Also, experimental or theoretical information can, if desired, be inserted into the method to prescribe this internal structure, while no experimental information is needed for the wake position.

CHAPTER 3

SOLUTION PROCEDURE

3.1 Basic Formulation

A potential flow solver using a rapidly converging approximate factorization scheme, together with a finite volume discretization scheme is employed. The scheme, originally developed for a fixed wing, is described in Reference [24, 25].

First, a mapping is defined from physical (x, y, z) to computational (X, Y, Z) coordinates. A set of constant radial computational planes are defined. In each plane the airfoil is mapped to a segment on the real axis using the transformation described in Reference [26]. If the transformations are represented by a Jacobian matrix H, Equation (3) may be written in terms of transformed variables:

$$\frac{\partial}{\partial X}(\rho h U) + \frac{\partial}{\partial Y}(\rho h V) + \frac{\partial}{\partial Z}(\rho h W) = 0 \qquad (4)$$

where U, V, W are contravariant velocities, and h is the transformation Jacobian,

$$h = det\ (H)$$

The physical velocity components, in terms of the potential and vortical velocities, are:

$$\vec{q} = \begin{pmatrix} u \\ v \\ w \end{pmatrix} = \left(H^T\right)^{-1} \begin{pmatrix} \phi_X \\ \phi_Y \\ \phi_Z \end{pmatrix} + \vec{\Omega} \times \vec{r} + \vec{q}^{\,v} \qquad (5)$$

where only derivatives of the potential with respect to the computational coordinates are required. The contravariant velocities are then calculated in terms of physical velocities.

$$\begin{pmatrix} U \\ V \\ W \end{pmatrix} = H^{-1} \begin{pmatrix} u \\ v \\ w \end{pmatrix}$$

H is given by

$$H = \begin{pmatrix} x_X & x_Y & x_z \\ y_X & y_Y & y_z \\ z_X & z_Y & z_z \end{pmatrix}$$

Equation (4) can now be represented as a flux balance relation. For this purpose, a secondary set of cells is introduced interlocking with the primary cells (Figure 4). In the computational domain the faces of the secondary cells span the midpoints of the primary cells. The purpose of the secondary cells is to serve as control volumes for the flux balance. The formula for the local flux balance can now be written using a second application of the scheme on the secondary cells. where Equation (4) is approximated by

$$\mu_{YZ}\delta_X\left(\rho hU\right) + \mu_{ZX}\delta_Y\left(\rho hV\right) + \mu_{XY}\delta_Z\left(\rho hW\right) = 0 \tag{6}$$

where the quantities ρhU, ρhV, and ρhW are the fluxes across the faces of the secondary cell. This formula is equivalent to calculating the flux across the part of a face of a secondary cell lying in a particular primary cell using the values for ρ, h, U, V, W calculated at the center of that primary cell.

3.2 <u>Grid Generation</u>

The grid is a particular type of "H" mesh. A two-dimensional grid is generated for each radial plane. The computational plane is first covered by an equally-spaced grid in the region

$$|X| \leq 1 - \delta$$

$$|Y| \leq 1 - \delta$$

where $\delta > 0$ is a small parameter that controls the far-field boundary position. A
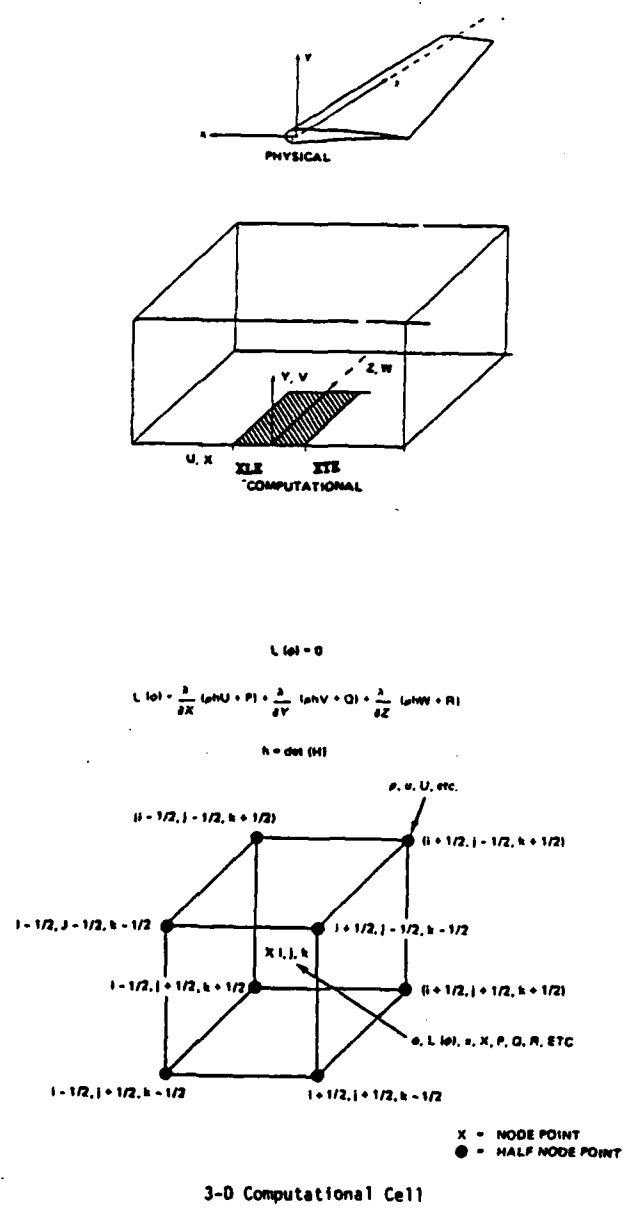
Figure 4: Coordinate System and Finite Volume Formulation

stretching is performed that maps X and Y from ± 1 to $\pm \infty$.

$$X' = c/2 + X^-/(1 - (X^-)^2/(1 - c/2)^2),$$

$$[+c/2 \leq X \leq 1 - \delta]$$

$$X' = X, \quad [-c/2 \leq X \leq c/2]$$

$$Y' = 1/2Y(1 - Y^2)$$

where,

$$X^\pm = X \pm c/2$$

and the airfoil is mapped to a segment on the real axis:

$$Y = 0 \quad [-c/2 \leq X \leq c/2,]$$

A square root transformation

$$z = Z'^{\frac{1}{2}} = (X' - iY')^{1/2} = R'^{\frac{1}{2}} e^{i\theta'/2}$$

is used to map the Z plane to the upper half plane (Z).

The same transformation is then used to map the airfoil to a curve about the real axis in the z plane. Next, a shearing transformation, $f(z)$, is defined in the $Im(z)$ direction such that this is mapped to a segment of the real axis. The physical plane coordinates are then computed by subtracting $f(z)$ from the z plane coordinates of the computational points. To improve the resolution near the leading edge, a nonorthogonal transformation is used in the Z plane in place of the basic square root one:

$$z = \frac{R'}{a - \sqrt{R'}} \frac{a + \sqrt{c}}{\sqrt{c}} e^{i\theta'/2}$$

where a is a grid compression length scale.

This grid is then rotated to the desired pitch angle as described by the twist distribution of the rotor blade. Finally, a simple blending technique [27] is used to enforce the outer and periodic boundary conditions on the grid (Figure 5).

3.3 Discretization

The finite volume scheme of Reference [28] is used to discretize Equation (6). Two staggered grids are used. On one, $\rho, u, v, w, U, V, W, H,$ and h are defined; on the other, $x, y, z, X, Y, Z, \phi,$ and $L_0(\phi)$ are defined. The nodes of each grid are at the centers of the cell of the other, and a box scheme is used to compute the derivatives in Equation (5) and Equation (6). For a variable f, we define

$$\delta_X f|_{i+\frac{1}{2},j+\frac{1}{2},k+\frac{1}{2}} = [f_{i+1,j+1,k+1} + f_{i+1,j,k+1} + f_{i+1,j+1,k}$$

$$+ f_{i+1,j,k} - f_{i,j+1,k+1} - f_{i,j,k+1} - f_{i,j+1,k} - f_{i,j,k}]/4$$

Similar expressions can be written for the Y and Z derivatives.

The basic finite volume scheme leads to an odd-even decoupling of solutions. If a small (higher order) term is added to the right hand side of the Equation (6), this problem can be eliminated. This can be easily seen by considering the case of incompressible flow in two dimensions. Setting $h = 1, \rho = 1$, Equation (6) reduces to

$$\mu_{YY} \delta_{XX} \phi + \mu_{XX} \delta_{YY} \phi = 0$$

where odd and even points are decoupled. It is due to the evaluation of flux across the face labeled AB in Figure 6 using a value of ϕ_X calculated at the point A.

COMPUTATIONAL GRID –CONSTANT R

NACA 0012 THETA =8 DEG. b =2
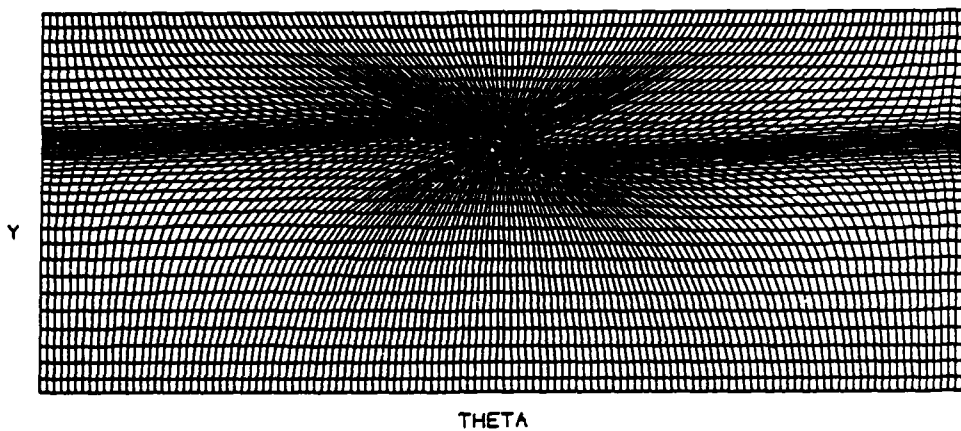
INNER PORTION OF   GRID

NACA 0012 THETA =8 DEG b=2

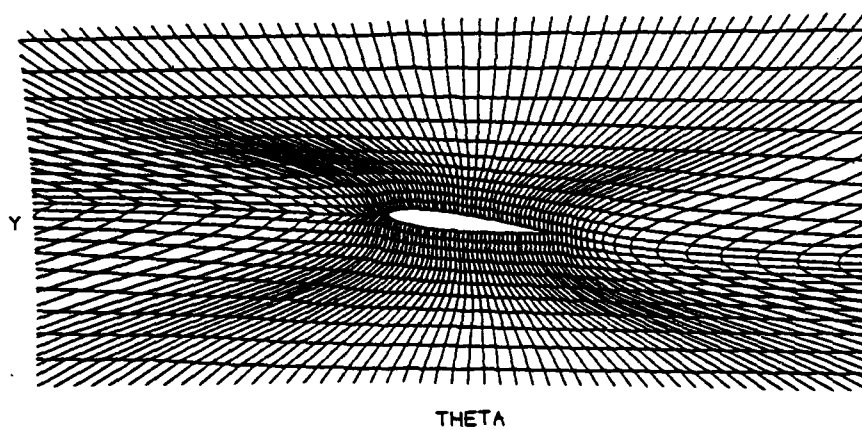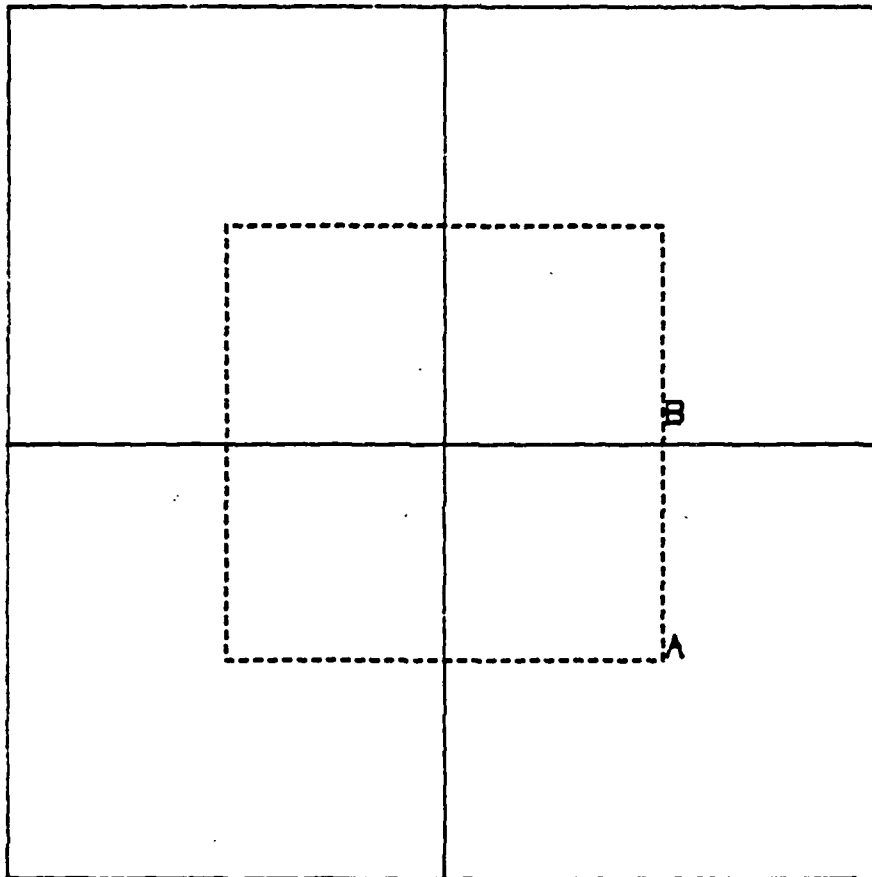Figure 5: Blended Rotor Grid

Figure 6: Schematic of Shift Evaluation for Compensation Flux Calculation

If a compensation flux, $\epsilon \Delta Y \phi_{XY}$, is added across AB, the point at which ϕ_X is effectively evaluated is shifted from A to B. The addition of similar compensation terms on all faces produces the scheme

$$\mu_{YY}\delta_{XX}\phi + \mu_{XX}\delta_{YY}\phi - \epsilon\delta_{XXYY}\phi = 0$$

The compensation terms for Equation (6) can be found in a similar manner [28]. These are

$$A = \rho h(g_{1.1} - U^2/a^2)$$

$$B = \rho h(g_{2.2} - V^2/a^2) \qquad (7)$$

$$C = \rho h(g_{3.3} - W^2/a^2)$$

Where $g_{i.i}$ are the diagonal elements of $(H^T H)^{-1}$.

Defining the following quantities

$$Q_{XY} = (A + B)\mu_z\delta_{XY}\phi$$

$$Q_{YZ} = (B + C)\mu_X\delta_{YZ}\phi$$

$$Q_{ZX} = (C + A)\mu_Y\delta_{ZX}\phi$$

$$Q_{XYZ} = (A + B + C)\delta_{XYZ}\phi$$

Equation (6) can be written with recoupling terms as:

$$\mu_{YZ}\delta_X(\rho hU) + \mu_{ZX}\delta_Y(\rho hV) + \mu_{XY}\delta_Z(\rho hW) +$$

$$\epsilon[\mu_z\delta_{XY}Q_{XY} - \mu_X\delta_{YZ}Q_{YZ} + \mu_Y\delta_{ZX}Q_{ZX} - \frac{1}{2}\delta_{XYZ}Q_{XYZ}] = 0 \qquad (8)$$

where

$$\delta_{XYZ}f = [f_{i+1,j+1,k+1} - f_{i,j+1,k+1} - f_{i+1,j,k+1}, -f_{i,j,k+1}$$

$$-f_{i+1,j+1,k} + f_{i,j+1,k} + f_{i+1,j,k} - f_{i,j,k}]$$

$$0 \leq \epsilon \leq 1/2$$

For stability in supersonic zones either a first order or a second order artificial viscosity can be used. For the first order form a switching function is defined:

$$s = max \left(0, 1 - \frac{M_C^2}{M^2}\right)$$

where M_C is the switching Mach number, taken to be slightly less than 1.

Then, from Reference [25],

$$P = \mu(U^2 \delta_x^2 \phi + \frac{UV}{4} \delta_{XY} \phi + \frac{WU}{4} \delta_{ZX} \phi)$$

$$Q = \mu(V^2 \delta_Y^2 \phi + \frac{VW}{4} \delta_{YZ} \phi + \frac{UV}{4} \delta_{XY} \phi)$$

$$R = \mu(W^2 \delta_z^2 \phi + \frac{WU}{4} \delta_{ZX} \phi + \frac{VW}{4} \delta_{YZ} \phi)$$

$$\mu = csh\rho^2/a^2$$

In this, P, Q, and R are constructed so that

$$P \text{ approximates } - \mu|U|\delta_x \rho$$

$$Q \text{ approximates } - \mu|V|\delta_Y \rho$$

$$R \text{ approximates } - \mu|W|\delta_z \rho$$

In the numerical scheme Equation (8) is modified by the addition of the terms

$$\delta_x P + \delta_Y Q + \delta_z R$$

Finally, an iterative scheme has to be devised for solving the discretized equation. This is accomplished by embedding the steady state equation in an artificial time dependent equation [29]. Such a process has to be carefully controlled to ensure stability and convergence. It is helpful to regard the iterations as successive levels

in an artificial time coordinate. The essential idea is that the iterative procedure, regarded as a finite difference scheme for a time dependent process, should be consistent with a properly posed initial value problem which is 'compatible' with the steady state equation; that is to say, that the solution of the initial value problem should reach an equilibrium point which represents a solution of the steady state equation. Then, if the difference scheme is also stable, it should converge to the desired solution.

Considering first the two dimensional case, the full potential equation can be written in canonical form:

$$(1 - M^2)\phi_{ss} + \phi_{nn} = 0 \tag{9}$$

where s and n are coordinates in the local stream and normal directions and

$$\phi_{ss} = \frac{1}{q^2}(u^2\phi_{xx} + 2uv\phi_{xy} + v^2\phi_{yy})$$

$$\phi_{nn} = \frac{1}{q^2}(v^2\phi_{xx} - 2uv\phi_{xy} + u^2\phi_{yy})$$

In the finite difference form for Equation (9), let updated values of potential ϕ at any level of the calculation be denoted by the superscript $+$. Then the typical central difference formula for a second derivative in the streamwise direction can be written as

$$\phi_{xx} = \frac{\phi_{i-1,j}^+ - (1 + r\Delta x)\phi_{ij}^+ - (1 - r\Delta x)\phi_{ij} + \phi_{i+1,j}}{\Delta x^2}$$

Where the updated value is used on one side, the old values on the other side (because the updated value is not yet available), and a linear combination of the two is used at the center point. In the time dependent system this formula may be interpreted as representing:

$$\phi_{xx} - \frac{\Delta t}{\Delta x}(\phi_{xt} + r\phi_t) .$$

With a similar representation, Equation (9) can be recast as a time dependent equation which contains mixed space-time derivatives;

$$(1 - M^2)\phi_{ss} - 2\alpha\phi_{st} + \phi_{nn} - 2\beta\phi_{nt} = 0$$

The values of α and β depend on the combination of new and old values actually used in the difference formulas. While interpreting the difference scheme as the representation of a time dependent process, it can be seen from stability analysis that the presence of a ϕ_t term can lead to instability at supersonic points [30]. This is in contrast to the subsonic part of the flow. There, the damping due to ϕ_t plays a critical rule in the convergence of the relaxation scheme.

The relaxation schemes have to be devised based on these principles, extended to three dimensions. For our equations, we solve a discrete approximation to

$$\delta_x (\rho h U + P) + \delta_Y (\rho h V + Q) + \delta_z (\rho h W + R) = \alpha\phi_{XT} - \beta\phi_{YT} + \gamma\phi_{ZT} + \delta\phi_T \quad (9)$$

In this care should be taken to have δ zero at all hyperbolic points. To solve this system of equations we have used an Approximate Factorization scheme that is described in the following section.

3.4 AFZ Scheme

During each iteration of the cycle a rapid approximate factorization method is used to solve Equation (8) with $\vec{q}^{\,v}$ fixed. The factorization is used in two-dimensional cylindrical (constant r) surfaces about the rotor axis. The angular extent of the grid on these surfaces depends on the number of blades present. The grid is periodic at the two vertical edges and the potential and $\vec{q}^{\,v}$ are also forced to be periodic there.

The basic idea behind the AFZ scheme is to solve a set of implicit equations in each constant radius plane, for a correction to ϕ. Since no implicit equations are solved in radial direction, the three dimensional array of ϕ values can be stored on disk and only several $\theta - y$ planes of data need be stored in the computer at any one time.

In Figure 7, the marching direction in the computational plane is shown. The equations are solved separately in each half plane (upper and lower) with boundary conditions that ensure continuity across the interface at convergence. During the iteration sweep number $n + 1$, when updating plane number k, values of ϕ are available corresponding to iteration $n + 1$ in plane $k - 1$ since it has just been updated. Only the updated (level n) values are available in planes k and $k + 1$. It was decided to make use of the available updated values in calculating residual at plane k. It is most efficient to compute contravariant velocities only once each iteration between each plane and use them in computing $L_0(\phi)$ for both planes on either side. To directly incorporate updated values of ϕ into each $L_0(\phi)$ computation, it would be necessary to abandon this approach and recompute these velocities, using them only once for each computation. This would almost double the number of calculations. An alternative, which was chosen instead, involved adding the correction multiplied by an appropriate constant to $L_0(\phi)$, computed using only old values at each plane. The final factorized scheme can be written as

$$N_{xy} \delta\phi^n = \alpha\omega L(\phi^n) + \alpha\omega \widetilde{C} E_z^- \delta\phi^n$$

$$\phi^{n+1} = \phi^n + \delta\phi^n. \tag{10}$$

where N_{xy} is an operator in the XY plane, α is an operator in the supersonic zone and a number in the subsonic zone, ω is a relaxation factor and E_z^- is the

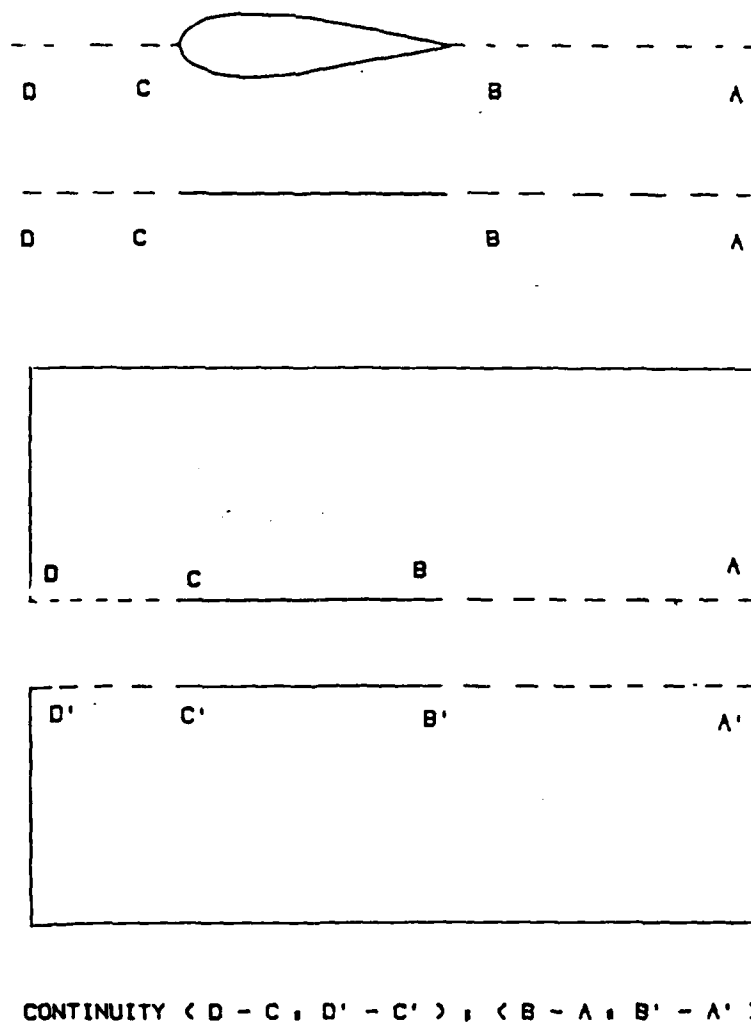CONTINUITY (D - C , D' - C') , (B - A , B' - A')

Figure 7: Computational Plane Coordinate System

shifting operator:

$$E_z^- \delta\phi_k = \delta\phi_{k-1}$$

N_{XY} was chosen from a successful two dimensional ADI scheme [30];

$$N_{XY} = (\alpha_X - \delta_X A \delta_X)(\alpha_Y - \delta_Y B \delta_Y) \tag{11}$$

The values of A and B are given by Equation (7). Also, α_X and α_Y are numbers at subsonic speed, and become operators for supersonic flow.

To approximate first order artificial viscosity terms

$$\alpha_X = \alpha - \delta_X^- \ \mu U^2 \delta_X^2$$

$$\alpha_Y = \alpha$$

For flow in the $+X$ direction (in this mapping there is no flow in $-X$ direction in the computational plane):

$$\alpha = \alpha_0 + \alpha_1 \delta_X^-$$

where

$$\alpha_0 = \ max \ (\beta_0, \beta_1)$$

$$\beta_0 = P_1 \ \Delta Z \ r(Z) \ max \ (0, 1 - \frac{q^2}{a^2})$$

$$\beta_1 = 2 \ P_1 \ r(z) \ \widetilde{C}$$

$$\alpha_1 = P_4 \ P_1 \ \Delta Z \ r(Z) \ min(1, \frac{q^4}{a^4})$$

$$\alpha_2 = P_5 \ P_1 \ \Delta Z \ r(Z) \ min(1, \frac{q^4}{a^4})$$

$$\widetilde{C} = P_2 \ \alpha_0$$

$$r(Z) = 1 + r_k/r_{tip}$$

P_1 - P_5 are ADI parameters. The relaxation factor ω is given by

$$\omega = P_3(1 + 1/r(Z))$$

The form of α_0 was chosen to become small when the local Mach number approached 1, which is required for stability. The use of $1/r(Z)$ in the formula for ω results in a relative under-relaxation for larger values of r, which further increases stability and improves convergence.

The solution sequence consists of a set of cycles. In each cycle there are k sweeps through the field, in which values of P_1 are cycled and set equal to $P_1^0, eP_1^0, e^2P_1^0 \cdots e^{K-1}P_1^0$, where e is a constant. All other parameters are kept constant. Best results were found for $K = 4$ and $e = \frac{1}{2}$ for fine grid calculations. In each sweep the factorized equations are solved plane-by-plane starting from the root, for corrections $\delta\phi$, which are added to ϕ. In each plane, first

$$(\alpha_x - \delta_x A\delta_x)\widetilde{\phi} = \alpha\omega\widetilde{C}E_z^-\delta\phi^n + \alpha\omega L(\phi)^n$$

is solved row-by-row for a temporary two-dimensional variable $\widetilde{\phi}$. Then,

$$(\alpha_Y - \delta_Y B\delta_Y)\delta\phi = \widetilde{\phi}$$

is solved column-by-column for the corrections $\delta\phi$.

3.5 Vortical Velocity Calculation

The calculation of $\vec{q}^{\,v}$ involves two parts: first the vortex sheet position is integrated as a set of marker streamlines to follow the flow using interpolated values of $\vec{q}$ from the fixed grid; then, from these marker positions $\vec{q}^{\,v}$ is computed. As discussed in section 2.3.3 in the decomposition of the potential and vortical

components, the vortical component, $\vec{q}^{\,v}$, is not unique. The basic idea is to spread the sheet into a thin vorticity region described by an appropriate velocity distribution, $\vec{q}^{\,v}$.

After solving for ϕ as described in Section 3.4, a velocity

$$\vec{q} = \vec{\nabla}\phi + \vec{q}^{\,v}$$

is computed at the grid points. The velocity is then interpolated to the marker locations. This is done by using a bilinear interpolation of the velocities at the four nearest grid points to each marker location (Figure 8). The markers are defined at each θ-like grid plane (approximately constant θ). Values of r and y are computed for each marker using a forward Euler integration scheme marching from one θ-plane to the next.

$$\vec{r}_v(s + \Delta s) = \vec{r}_v(s) - \Delta S \times \vec{q}(\vec{r}_v) \qquad (12)$$

In Equation (12) $\vec{r}_v(s)$ is the current marker position. $\vec{q}(\vec{r}_v)$ is the interpolated velocity at the marker location. To generate the sequence of values for $\vec{r}_v(s)$, it is necessary to determine which computational cell each vector is in and compute an interpolated value of $\vec{q}(\vec{r}_v)$ using values of $\vec{q}$ at corners of that cell. A simple test on r is used to determine the r-plane, or K index of the cell. The other indices required tests on the cross products between vectors from the corners of the cell and $\vec{r}_v$ and vectors between adjacent corners. For example, if the current $\vec{r}_v(S = S_0)$ were in cell (j,k), a test that it had crossed into cell $(j + 1, k)$ upon integration over one step is that the θ component of the cross product,

$$.C(s) = (\vec{r}_{j+1,\,k} - \vec{r}_{j+1,\,k+1}) \times (\vec{r}_v(s) - \vec{r}_{j-1,\,k-1})$$

changed sign. That is,

$$C(S_0)_\theta \times C(S_0 + \Delta S)_\theta < 0$$
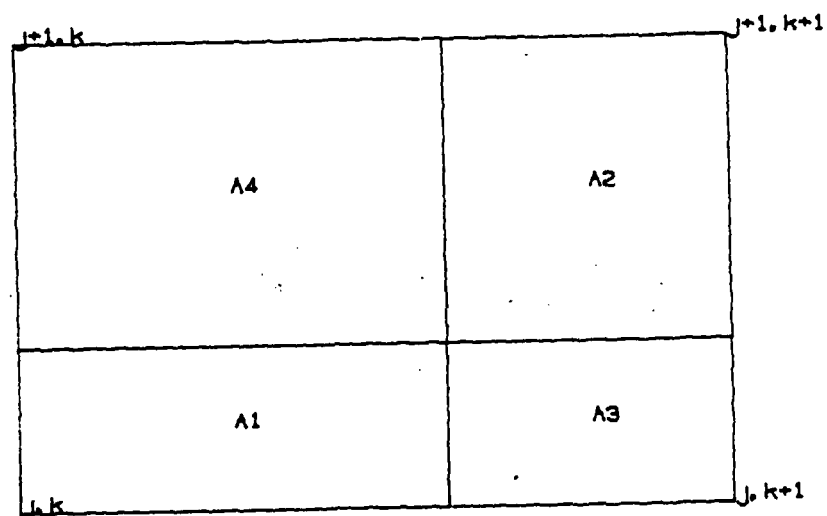
$$A - A_1 + A_2 + A_3 + A_4$$

$$f - (f_{j,k} A_2 + f_{j,k+1} A_4 + f_{j+1,k} A_3 + f_{j+1,k+1} A_1)/A$$

Figure 8: Bilinear Velocity Interpolation

Finally, the step size ΔS is determined using the interpolated value of $\Delta \Theta$ and $r\dot{\Theta}$ (tangential velocity) at the marker locations. ΔS is given by

$$\Delta S = \frac{\Delta \Theta}{r\dot{\Theta}}$$

The values of $\Delta \Theta$ are obtained at the grid points using the values of Θ at the $(i+1)$ plane and the i plane. Once $\vec{r}_v(S + \Delta S)$ is calculated using Equation (12), the solution is advanced to the $i+1, \Theta$-plane. The procedure is repeated until the markers reach the end of the grid, determined by $\Theta_{max} = \frac{\pi}{N_b} (-\Theta_{max} \leq \Theta \leq \Theta_{max})$. In hover the effects of other blades could be exactly accounted for by setting periodic boundary conditions at proper angles given by Θ_{max}. Also the other spiral turns of the vortex sheets can be computed by relocating the markers at the upstream edge, $(+\Theta_{max})$ at the same radial and axial position where they leave the downstream edge $(-\Theta_{max})$.

No instabilities were observed in regions of large step sizes. Thus, a large number of sheets can be computed and this is restricted only by the axial extent of the grid and computer memory related restrictions. In general, an azimuthal length of two and a half times the azimuthal distance between neighboring blades is used for computation. A computed wake geometry for a two bladed rotor and a four bladed rotor are shown in Figure 9 and Figure 10, respectively.

Once the set of $\vec{r}_v$'s are computed the vortical velocity, $\vec{q}^{\,v}$ can be computed. $\vec{q}^{\,v}$ can take many forms, as long as it has the correct vorticity. The best type of $\vec{q}^{\,v}$ for this purpose is the one which is concentrated near the line of vorticity, so that corrections to the potential equation are limited to a relatively small region. The tangential velocity changes rapidly and normal velocity is small near the sheet, and a $\vec{q}^{\,v}$ was initially sought with these properties. In this type of representation a
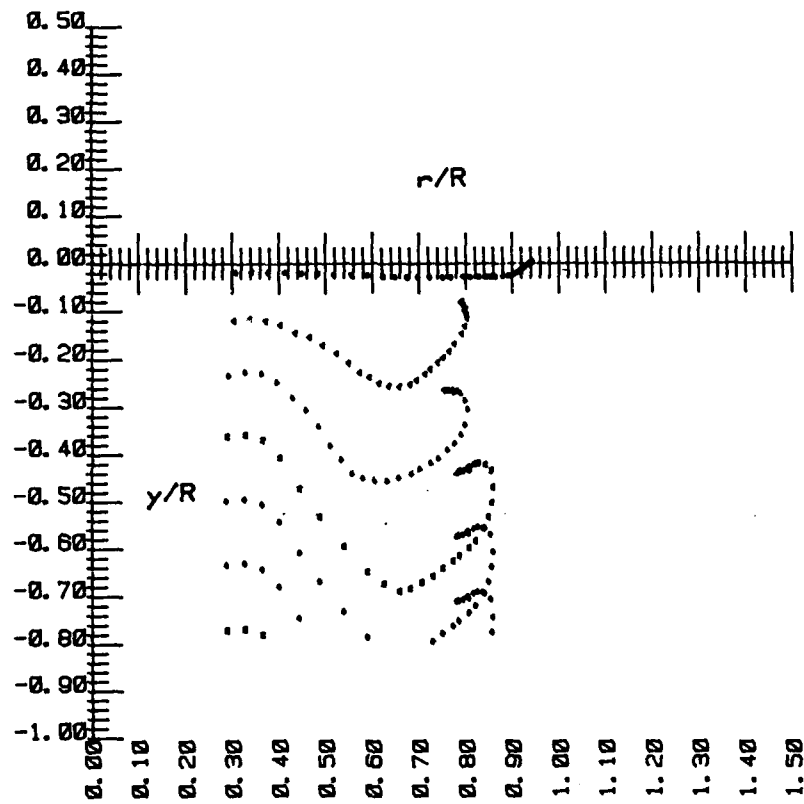
Figure 9: Cross Section of Wake Geometry for Two-Bladed Rotor

r

0. 50
0. 00
0. 50
1. 00
1. 50
2. 00
2. 50
3. 00

Y

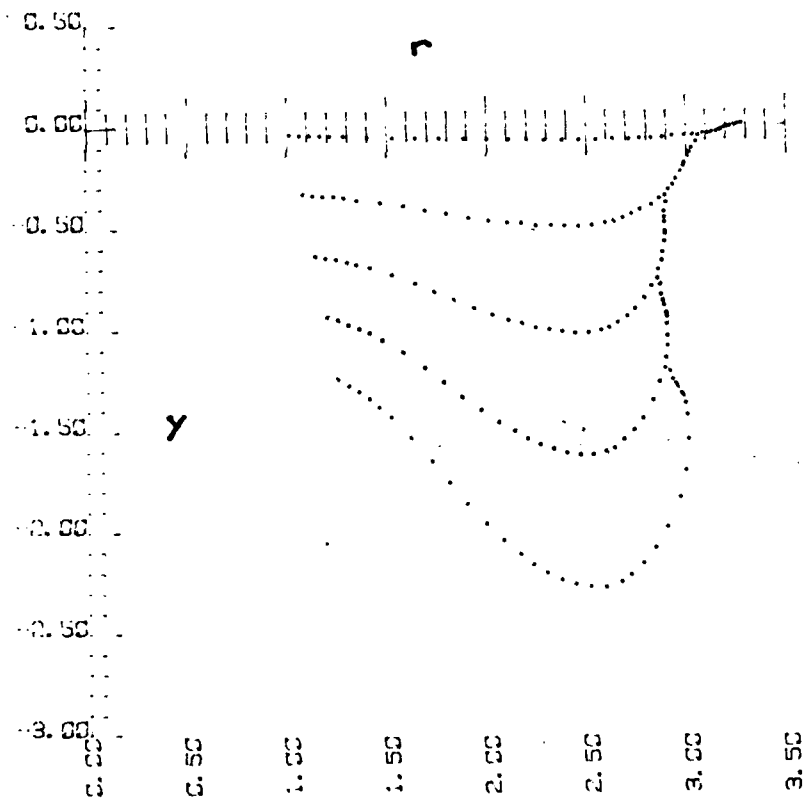0. 00   0. 50   1. 00   1. 50   2. 00   2. 50   3. 00   3. 50

Figure 10: Cross Section of Wake Geometry for Four-Bladed Rotor

tangential velocity discontinuity is being replaced by a region of spread tangential velocity variation. While this is a good picture for the total velocity, $\vec{q}$, it would be a bad choice for $\vec{q}^{\,v}$. This is due to the fact that such a tangential $\vec{q}^{\,v}$ must extend throughout the entire flow field. Even though the $\vec{\omega}$ field is nonzero in only a small region, this particular $\vec{q}^{v}$ field (which defines $\vec{\omega}$) is not small nor limited to a small region, and requires a large amount of memory. Denoting the direction along the normal to the sheet by n and along the line by s,

$$\vec{\omega} = \partial_s \vec{q}_n - \partial_n \vec{q}_s = \partial_s \vec{q}_n^{\,v} - \partial_n \vec{q}_s^{\,v} \tag{13}$$

Since $\vec{\nabla}\phi$ does not contribute to $\vec{\omega}$. Thus, if $\vec{q}_n^{\,v} = 0$ and if q_s^{v} goes to zero away from the line,

$$\partial_n q_s^{v} = -\vec{\omega} \neq 0$$

Hence, a $\vec{q}^{\,v}$ oriented along the sheet must be extended throughout the field if the vorticity is to be concentrated only near the sheet.

Another, more computationally efficient approach is to use a distribution of spread velocity normal to the sheet surface as shown in Figure 11. If $q_s^{v} = 0$ and $q_n^{v} \neq 0$, however. $\vec{\omega} = \partial_s q_n^{v}$ and q_n^{v} can be concentrated near the sheet, going to zero away from it. Thus, instead of point vortices the sheet is considered to be made up of a set of discrete velocity vectors oriented normal to the line within the cross-plane and concentrated near it. Then $\vec{q}^{\,v}$ is non zero only in a small region near the sheet. This representation seems very unphysical until one considers that it is not the entire velocity which is represented. but merely the vortical portion, $\vec{q}^{\,v}$. The total velocity, $\vec{q}$ must still be of the form shown in Figure 12. after the potential part, $\nabla\phi$ is added. The vortical part $\vec{q}^{\,v}$, can have any form as long as $\vec{\omega} = \nabla \times \vec{q}^{v}$. The normal form depicted in Figure 11 has the advantage of being nonzero only in a thin region, just like $\vec{\omega}$.
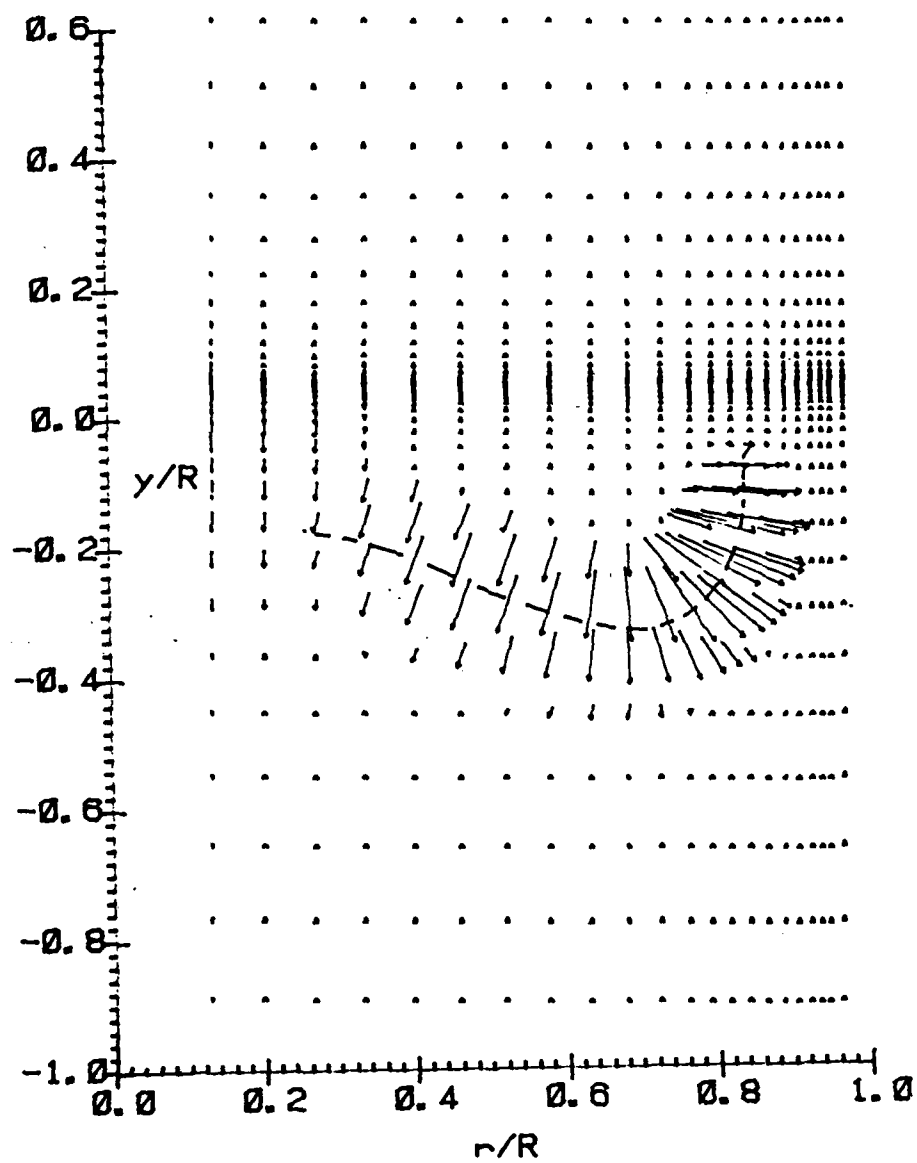
Figure 11: Vortical Velocity Distribution for the third sheet of Figure 10
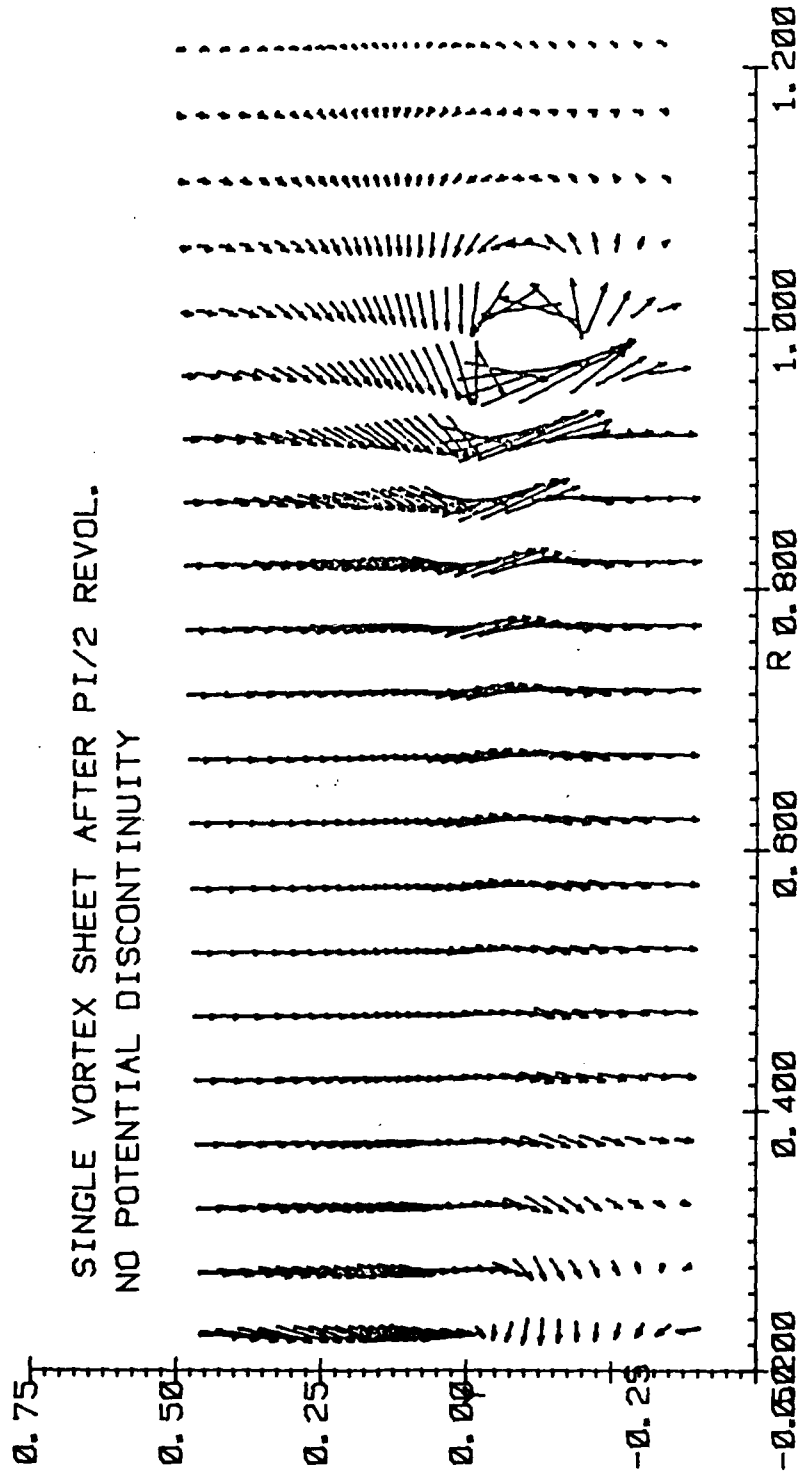
43

Figure 12: Velocity in a Cross-Plane

The advantage of this type of representation is twofold:

1. It is possible to give a structure to the vorticity field $\bar{\omega}$. This field can be *either solved for or modeled*.

2. It is possible to put vorticity anywhere in the field with no constraints imposed by the grid.

With these features, a combined Eulerian-Lagrangian code has been developed for the hover problem. The vortical velocity component, $\vec{q}^{\,v}$, is a normal velocity distribution describing a thin shed vorticity sheet which is allowed to convect freely through the flow field. $\vec{q}^{\,v}$ is a continuous vortical velocity field which suffers no artificial numerical diffusion and can easily be tailored to the problem. For the hover problem it has sufficed to model $\vec{q}^{\,v}$ using functions which were chosen on the basis of numerical convenience alone.

In order to find the required strength of $\vec{q}^{\,v}$ we use Gauss' theorem to obtain a relation for the integral of $\vec{q}^v$ along a normal at each point on the sheet;

$$\int q_n^v dn = \Gamma$$

The circulation, Γ, is known at the upstream edge of the sheet (blade trailing edge) from the lift distribution (which is computed as part of the entire calculation). Since it is constant along mean streamlines within the sheet it can easily be computed on the entire sheet. This relation provides a scaling factor which gives the magnitude of $\vec{q}^{\,v}$ as soon as the width of the layer and the functional form of $\bar{\omega}$ is determined. This width and functional form can be found by using a viscous solution or by simply choosing apropriate values. For the rotor wake problem, the latter approach suffices. These vectors are convected with the flow, and as the

line evolves and the distance between vectors changes, the magnitude of the $\vec{q}^{\,v}$ vectors (q_n^v) is changed so that the averaged q_n^v remains constant at each position on the line. To avoid singularities q_n^v is spread over a small region, comparable to the mesh spacing on either side of the line:

$$\vec{q}^{\,v}(\vec{r}) = C \sum_\ell \Gamma_\ell \, \sigma(|\vec{r} - \vec{r}_\ell|)\vec{q}_\ell^{\,v}$$

where Γ_ℓ is the circulation at the trailing edge where the particular marker (ℓ) originated, the spreading function,

$$\sigma(\Delta r) = max(0, 1 - \frac{\Delta r^2}{a^2})$$

and $\vec{q}_\ell^{\,v}$ is a vector normal to each panel and proportional to the panel area. The normalization constant C is such that, in the limit when markers are closely spaced and Γ_ℓ is slowly varying, the integral of $\vec{q}^{\,v}(\vec{r})$ through the sheet at any marker, m, equals to Γ_m. The only specified quantity is "a" which is taken to be about two cell widths. Stable, smooth solutions have been found using this spreading.

Referring to Figure 13, the closed line integral of $\vec{q} \cdot d\vec{\ell}$ around a portion of the sheet is equal to the area integral of ω_n. Since $\vec{\nabla}\phi$ does not contribute to the line integral and $\vec{q}^{\,v}$ is short range, only those portions of the line near the sheet encircled by dashed curves contribute to the integral. No matter how $\vec{q}^{\,v}$ is distributed along the sheet within the closed curve, the area integral of ω_n is determined by the two small areas where the path crosses, which are equal to the circulation corresponding to the markers at those points. The motion of the markers through the velocity field is determined by the requirement that the integral of momentum through the sheet is conserved. It is important to see that only such short-range (nonzero in only a few cells on either side of the sheet) $\vec{q}^{\,v}$'s can be effective for use in this scheme. If we had a long range form, given,
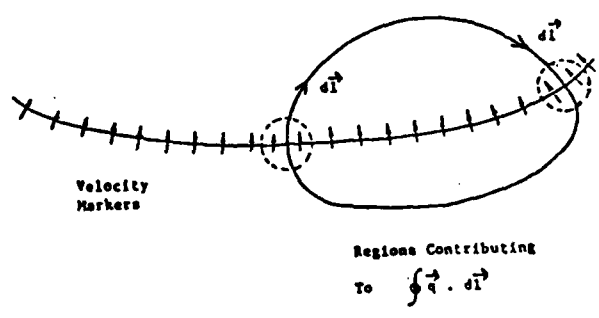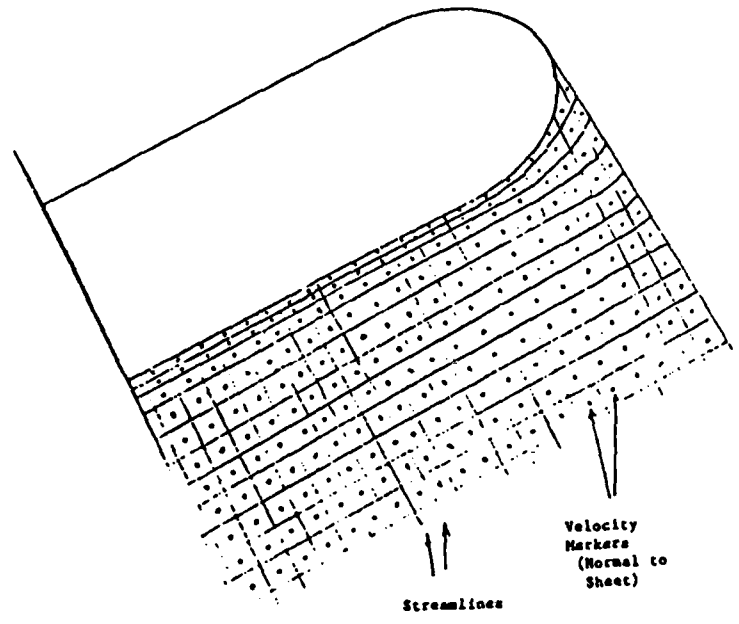
Figure 13: Schematic of Circulation Integral

for example, by the Biot-Savart law then the $\vec{q}^{\,v}$ calculation would have to be made for each point in the entire grid. Each of these would effectively involve a two dimensional integration over the entire vortex sheet, which would then be prohibitively expensive.

An interpretation of the $\vec{q}^{\,v}$ term for incompressible flow is as follows: considering a small region near the line, we can ignore the $\partial_s^2 \phi$ tangential terms in the Laplacian since $\partial_n^2 \phi$ will be much larger and we have,

$$\vec{\nabla} \cdot (\vec{\nabla}\phi + \vec{q}^{\,v}) = \nabla^2 \phi + \partial_n q_n^v = 0.$$

or

$$\nabla^2 \phi \simeq \partial_n^2 \phi = -\partial_n q_n^v$$

Hence,

$$\partial_n \phi = -q_n^v + constant$$

$$[\phi] = \int q_n^v dn.$$

where brackets denote the jump in ϕ across the line and the integral is done normal to and through the line. Thus we are effectively putting in a smeared discontinuity in ϕ. Exactly the same argument applies to the compressible potential flow case.

The vortical velocity is computed at each point in the grid where, $\vec{\nabla}\phi$ is computed using a spreading distance that is proportional to the local cell area for each sheet. Then, the contribution to $\vec{q}^{\,v}$ from each sheet at a given point is added to give the total $\vec{q}^{\,v}$.

3.5.1 Revised Formulation for Vortical Velocity Calculation

The calculations described above were done with an initial formulation described in Section 3.1. It can be shown that, as the grid is refined, the (specified) vortex spreading with this initial formulation must decrease less rapidly than the cell size. Otherwise, numerical effects appear which can be reflected in the motion of the vortex. For example, considering a blade segment with constant circulation, if the spreading is of the order of the cell size, h, and the spreading function is constant within h and zero outside,

$$|\vec{q}^{\,v}|\Gamma/h$$

if a grid point is within the spreading distance and zero otherwise.

The vorticity in a computational cell where only one point is within spreading distance of the sheet is then given by

$$|\vec{\omega}|h^2 = \int \vec{q} \cdot d\vec{\ell} = \frac{\beta}{2}|h\vec{q}^{\,v}|$$

Where α is the angle of orientation of the sheet and

$$\beta = cos\ \alpha - sin\ \alpha$$

From this,

$$|\vec{\omega}| = \beta\Gamma/2h^2$$

or

$$|\vec{\omega}| \sim 1/h^2$$

and the numerical error in velocity even in a region of zero

$$|\delta q| \sim 1/h$$

Thus, a numerical vorticity is created locally (when it should actually be zero for constant Γ) that increases as $\frac{1}{h^2}$. This also happens in regions where three corners of the cell are within the spreading distance and one outside.

A more accurate form for $\vec{q}\,^v$ based on Clebsch-type of representation has been developed and used on four-blade rotor configurations. In this formulation:

$$\vec{q}^v = \Gamma^c \vec{\nabla} \psi,$$

where $\Gamma^c(\vec{r})$ is a three dimensional field which smoothly goes to the appropriate Γ (circulation value) on the sheet as $\vec{r}$ approaches the sheet surface. The Clebsch potential, $\psi(\vec{r})$, smoothly goes from $+1/2$ on one side of the sheet to $-1/2$ on the other. A convenient formula for $\psi(\vec{r})$ is

$$\psi(\vec{r}) = 1/2 \; sin \; (\pi S_n/2), \quad |S_n| \leq a/2$$

$$\psi(r) = +1/2, \quad S_n > +a/2$$

$$\psi(\vec{r}) = -1/2, \quad S_n < -a/2$$

where S_n is a (signed) normal distance from the point $\vec{r}$ to the sheet.

We use interpolation-like formulae to compute $\Gamma^c(\vec{r})$ and $S_n(\vec{r})$ at any grid point $\vec{r}$;

$$\Gamma_c(\vec{r}) = [\sum_{\ell} \Gamma_{\ell} \sigma(\Delta \vec{r}_{\ell})]/A$$

$$\vec{S}_n(\vec{r}) = [\sum_{\ell} \vec{S}_{\ell}^n(\vec{r}, \vec{r}_{\ell}) \sigma(\Delta \vec{r}_{\ell})]/A$$

$$S_n(\vec{r}) = |\vec{S}_n(\vec{r})|$$

$$A = \sum_{\ell} \sigma(\Delta \vec{r}_{\ell}),$$

$$\Delta \vec{r}_{\ell} = \vec{r} - \vec{r}_{\ell}$$

where the Γ_l is the circulation defined for each marker, l, that defines the sheet. Γ_{ℓ} remains constant on each marker from the point on the blade trailing edge where

it is shed. Also, $S_\ell^n(\vec{r},\vec{r}_\ell)$ is the normal distance from $\vec{r}$ to a plane through the sheet at marker ℓ and the spreading function, $\sigma(\Delta\vec{r}_\ell)$ is

$$\sigma(\Delta\vec{r}_\ell) = max(0, 1 - \Delta\vec{r}_\ell/a^2)$$

where a is a specified spreading distance.

Even through ψ is non-zero throughout the field (except on the sheet), $\vec{\nabla}\psi$ is zero beyond the spreading distance from the sheet. Accordingly, both $\Gamma^c(\vec{r})$ and $\psi(\vec{r})$ need be computed only on those grid points that are in a narrow band about the sheet with thickness of the order of the spreading distance. With this $\vec{q}^{\,v}$ there is no spurious numerical vorticity in regions near the sheet where Γ is constant (no physical vorticity on the sheet), and even in regions where Γ varies smoothly there is no divergent error that becomes large as the grid is refined. In regions where Γ is constant $\Gamma^\ell(\vec{r})$ will be constant and $\vec{q}^{\,v}$ can be written

$$\vec{q}^{\,v} = \vec{\nabla}(\Gamma^c\psi(\vec{r})).$$

Even though $\vec{q}^{\,v}$ is still non-zero, if the same numerical differencing scheme is used for $\vec{\nabla}\psi$ as is used for $\vec{\nabla}\phi$, the effect of the sheet in regions of zero vorticity will be identically zero. This was not true for the earlier formulation of $\vec{q}^{\,v}$, and resulted in a requirement for larger spreading distances and thicker vortices (for a given grid). The new formulation has been successfully applied to two four-bladed rotor configurations and is seen to give improved vortex geometry. Vorticity contours for a four-blade rotor obtained using this revised formulation is shown in Figure 14. Also this formulation allows the embedding of a tighter vortex sheet with smaller spreading, even in a fairly coarse, computationally efficient mesh.
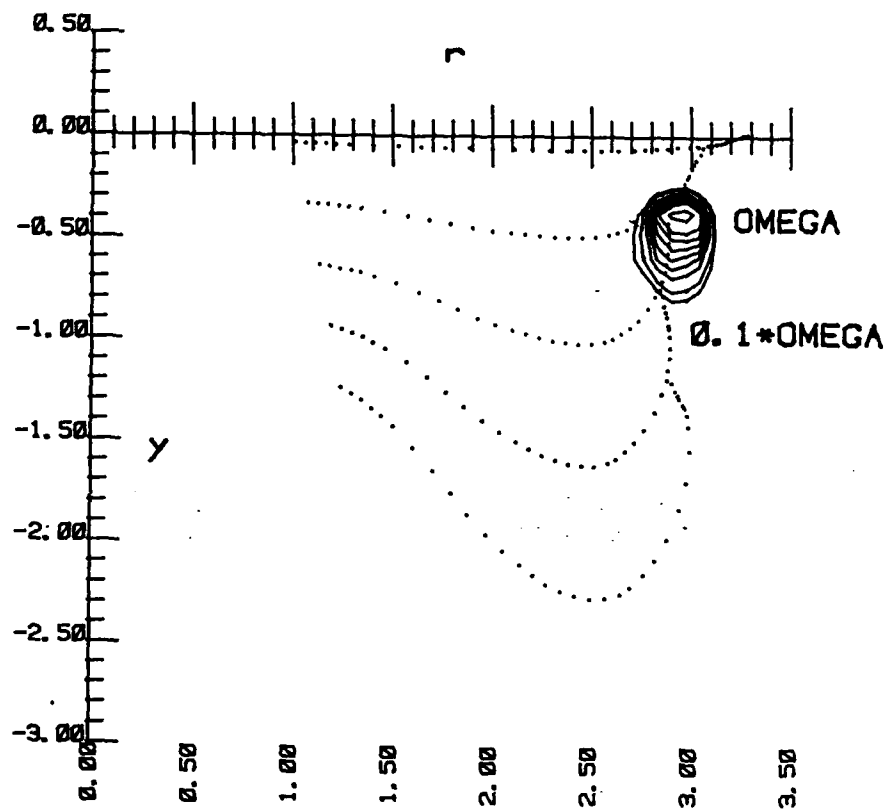
Figure 14: Wake Geometry and Vorticity Contour for the Third Sheet

3.6 Boundary Condition

For all of the results presented a 128 x 40 x 32 grid computational was used. The upper boundary is at about a half rotor span above the rotor disk. Dirichlet conditions were imposed on the potential there, using a form given in Reference [14] for a semi-infinite vortex cylinder, which approximates the vortex system at this boundary, given by

$$\phi_c = \frac{1}{4}\frac{d\Gamma}{dy}\left(\frac{r_{cyl}}{\sqrt{r^2 + (y - y_{cyl})^2}}\right)$$

where y_{cyl} is the position of the top of the cylinder. At the lower boundary, about 0.8 span below the rotor disk, a corrected periodic condition is imposed on both $\vec{q}^{\,v}$ and the potential. In this region the markers are descending at an approximately constant rate and the vortex sheet is approximately periodic in height (y). If this vortex system were infinite this velocity would be exactly periodic. A correction is required since the vortex system is only semi-infinite, starting approximately from the rotor plane. This correction involves adding a velocity similar to that used at the upper boundary.

At the blade surface, the normal velocity is zero, which implies

$$\partial_n\phi = -\vec{q}_n^{\,v}.$$

Finally, Dirichlet conditions are used at the outer cylindrical boundary.

CHAPTER 4

RESULTS

4.1 Comparison of Results for Two-Blade Rotors

Several applications have been completed which illustrate the predictive capabilities of the method. Some of the results reported for the two bladed rotors, were published in 1986 [32, 33, 34]. Results are presented for the full solution of a lifting rotor in hover, as computed by the three dimensional compressible flow code, **HELIX I** which has been developed. In Figure 12 preliminary results of the full three dimensional compressible code are presented for a single vortex sheet shed by a rotor blade. Here, the velocity in a cross-plane, normal to the blade motion, several chords behind the trailing edge is presented. The cross-stream velocity clearly shows a tight vortex which is the size specified by the model used. This remains the same as it is convected downstream. Other internal vortex structure and density distributions consistent with the grid spacing could be imposed. For this analysis, a rotor with an aspect ratio of 19, a constant pitch of 5^0 and Joukowski profile was used. Figure 15 depicts the vorticity contours for the separate contribution of each individual sheet for relative values of 0.45 and 0.7. The contour values are chosen to show the effect of the individual sheets as well as the spreading. Figure 16 presents the contours for the total vorticity field, which is a sum of individual sheet contributions.

The next two bladed rotor chosen for analysis was a high aspect ratio ($AR =$ 18.2) rotor with a constant 8^0 pitch and NACA0012 profile. Flow visualization
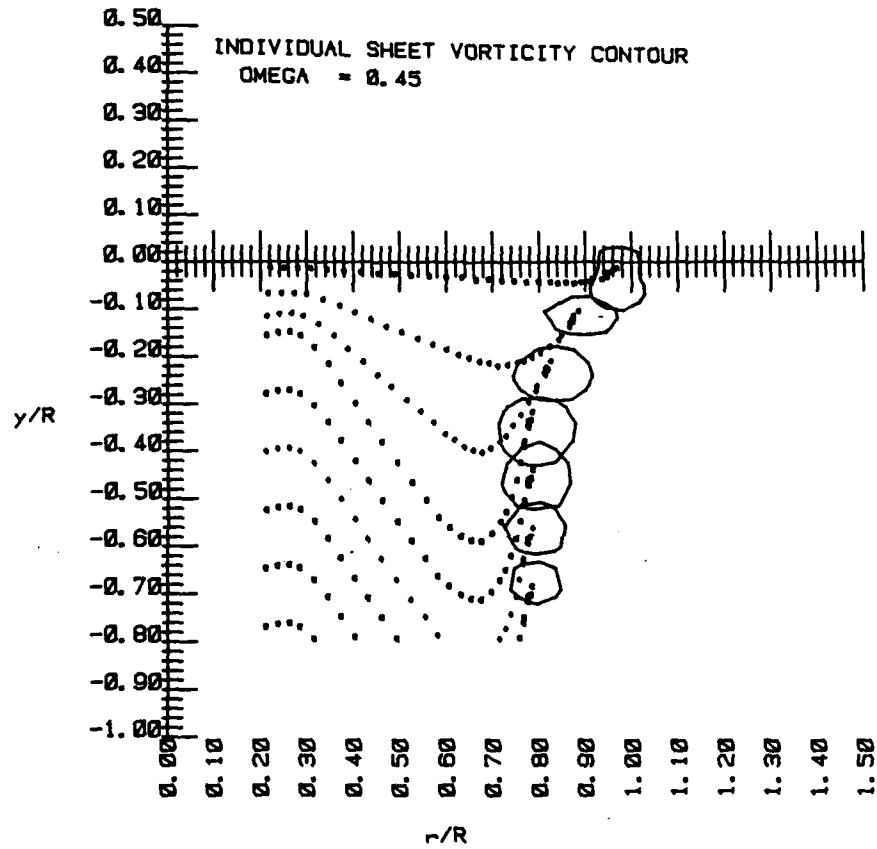
Figure 15: Individual Sheet Vorticity Contour

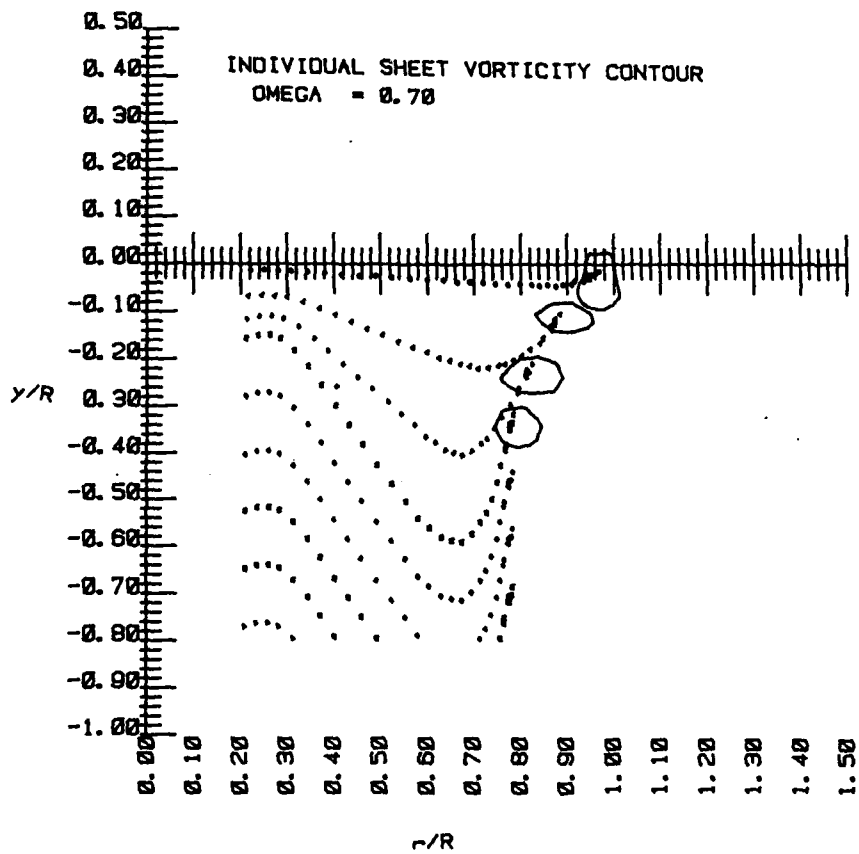INDIVIDUAL SHEET VORTICITY CONTOUR
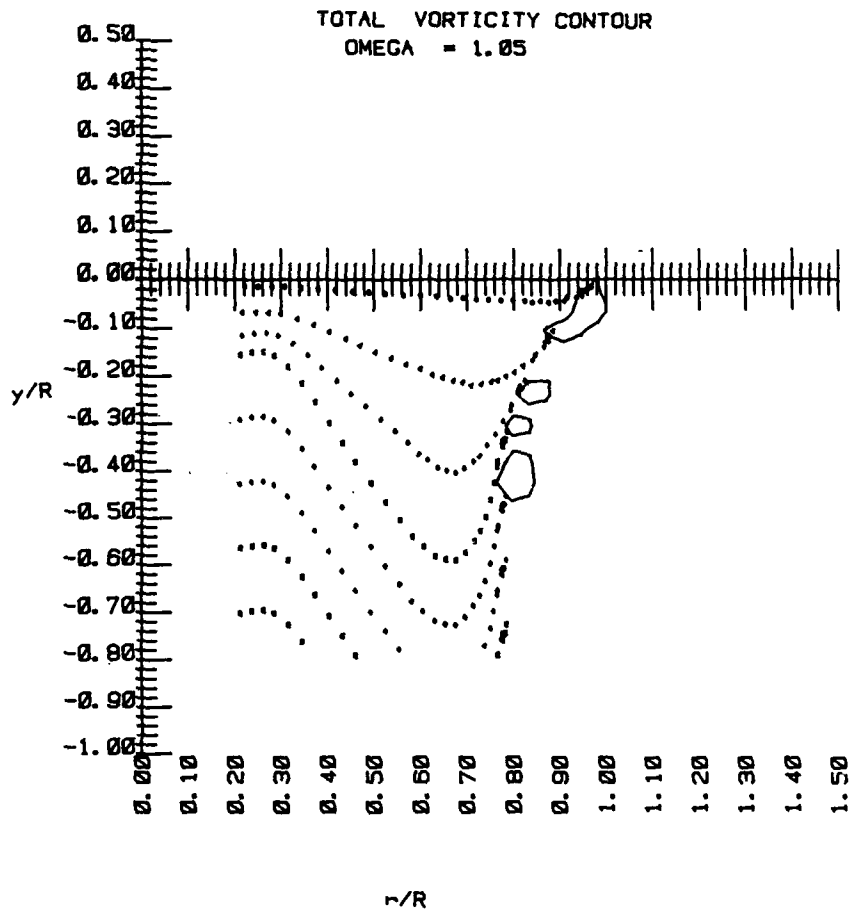OMEGA = 0.70

Figure 15: (continued)

Figure 16: Total Vorticity Contour

data are available for this rotor from Reference [4], and the calculated cases were matched to this reference. The computed wake geometry along with the experimental data in the form of tip vortex axial and radial coordinate are presented in Figure 17. The load distribution is presented in Figure 18 and chordwise pressure distribution at 68% and 89% span are presented in Figure 19.

A final two-blade rotor case has an aspect ratio of 6, NACA0012 profile with no twist or taper a collective pitch of 8^0. The experimental data used for comparison was obtained from Reference [35]. In this report a complete set of experimental data for chordwise pressure distribution, tip vortex geometry and spanwise load distribution was provided for a wide range of tip Mach numbers including transonic flow. Two tip speeds were considered in this computation: one subsonic $(M_{tip} = 0.436)$ and another transonic (0.877).

For the subsonic case, the computed wake geometry is presented in Figure 20 as the tip vortex radial coordinate and axial coordinate plotted as a function of vortex age. The experimental vortex geometry of Reference [34] is also presented in Figure 20. It can be seen that the computed vortex geometry compares favorably with experimental data. Also it can be observed from Figure 17 and Figure 20 that the wake parameter k (axial slope of the tip vortex trajectory before passage of the following blade) shows a strong dependence on aspect ratio. This is expected since for rotors of the same blade number and operating condition, both the disk loading C_T and inflow velocity will decrease with increasing aspect ratio, resulting in lower tip vortex settling rate. In Figure 21, the circulation distribution is presented. There is a relatively large increase in the normal loads due to the tip vortex shedding in the last 20% of the blade radius. This shows the importance of modelling of the tip vortex shedding for prediction of rotor loads. Chordwise
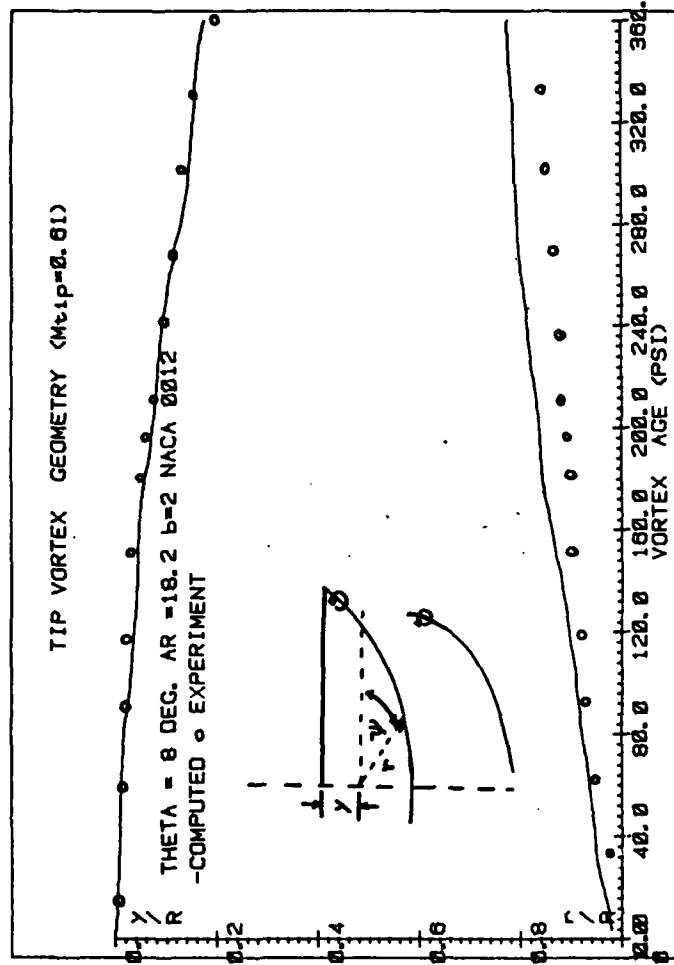
Figure 17: Comparison of Tip Vortex Coordinates for a High Aspect Ratio Two-Bladed Rotor at 8° Constant Pitch and NACA0012 Airfoil with Experimental Data of Landgrebe [4]
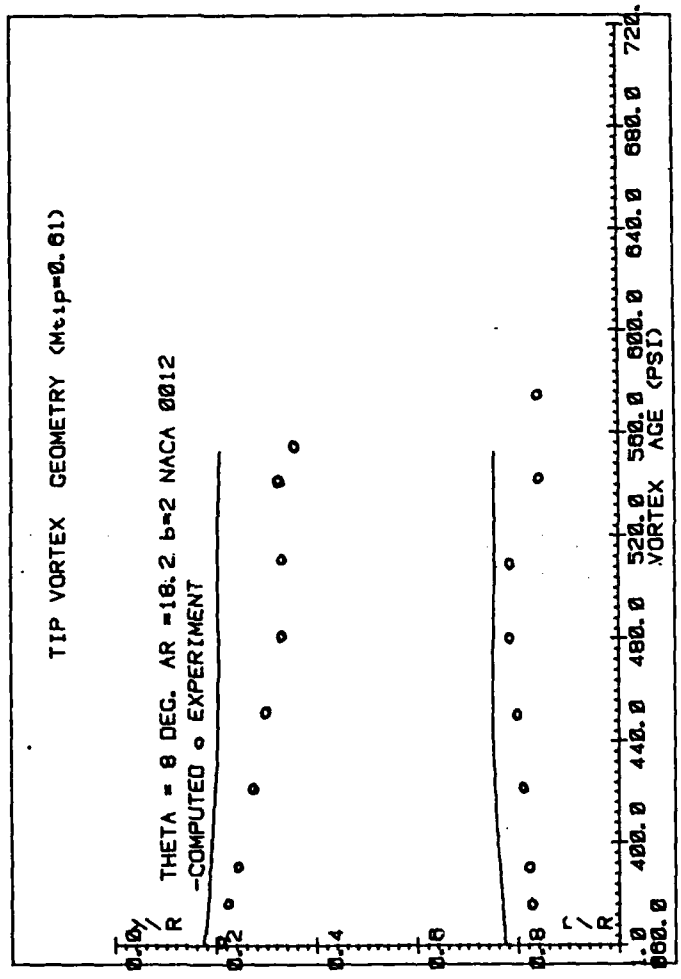
58

TIP VORTEX GEOMETRY (Mtip=0.61)

THETA = 8 DEG. AR =18.2 b=2 NACA 0012
—COMPUTED o EXPERIMENT
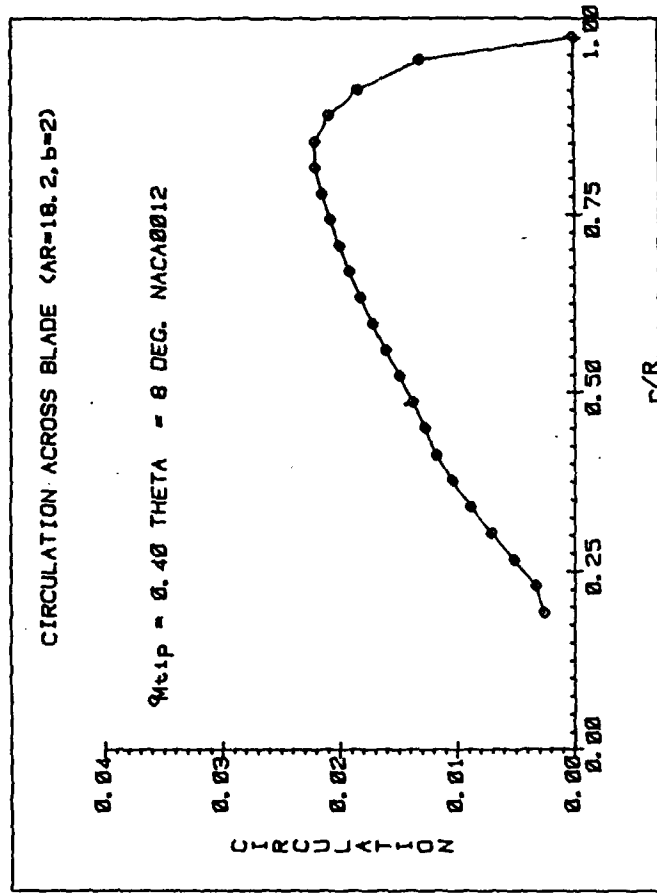
Figure 17: (continued)

60

Figure 18: Blade Circulation Distribution for High Aspect Ratio Two-Bladed Rotor with a Collective Pitch of 8⁰ and NACA0012 Profile
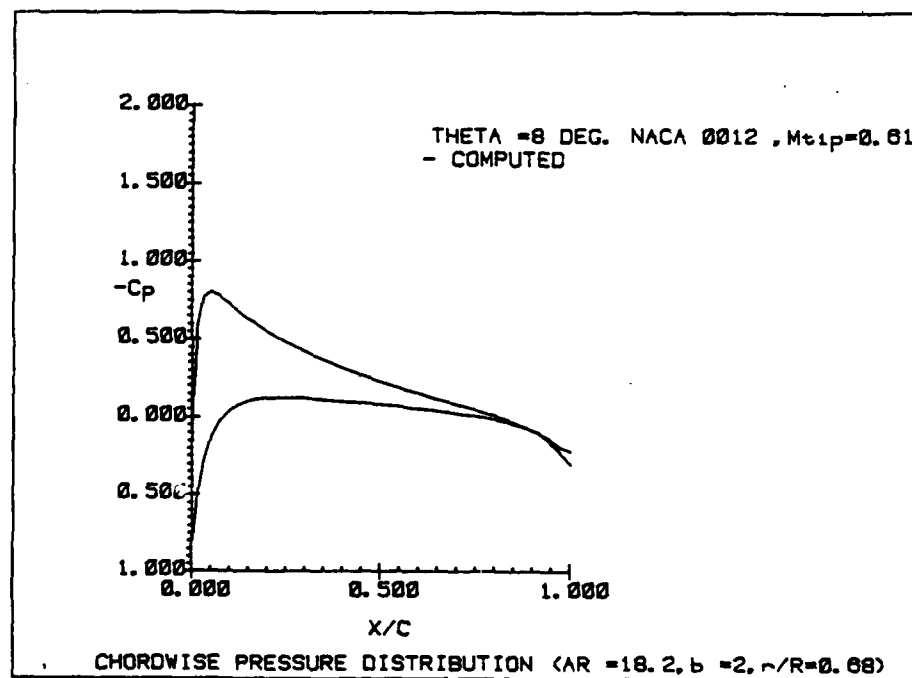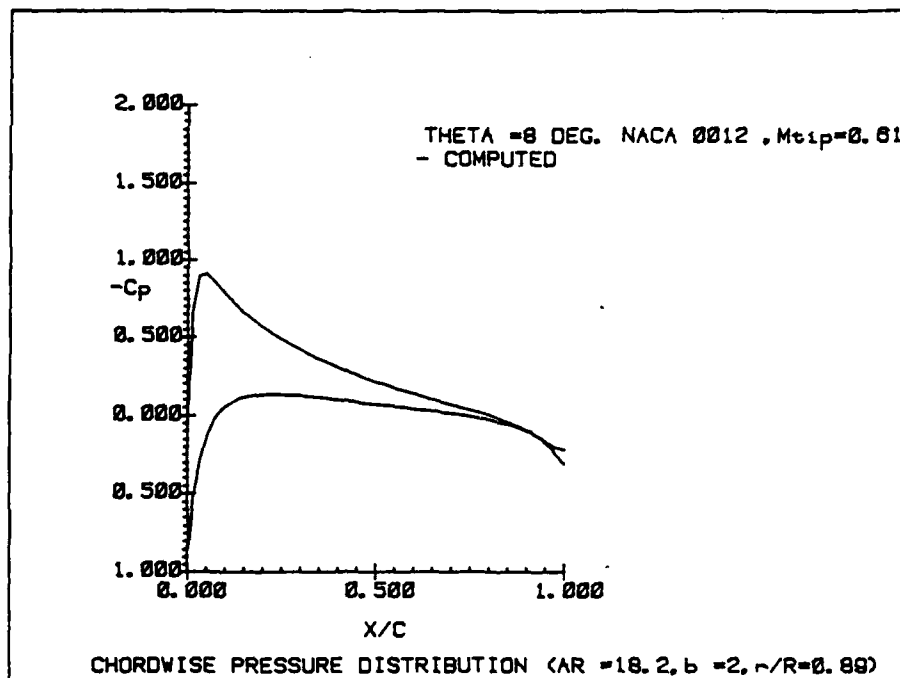
Figure 19: Computed Chordwise Pressure Distribution for High Aspect Ratio Two-Bladed Rotor with a Collective Pitch of 8° and NACA0012 Profile

TIP VORTEX GEOMETRY (Mtip=0.436)

THETA =8 DEG. AR =6 b=2 NACA 0012
− COMPUTED
o EXPERIMENT

−y/R

VORTEX AGE (PSI)

TIP VORTEX GEOMETRY (Mtip=0.436)

THETA =8 DEG. AR =6 b=2 NACA 0012
− COMPUTED
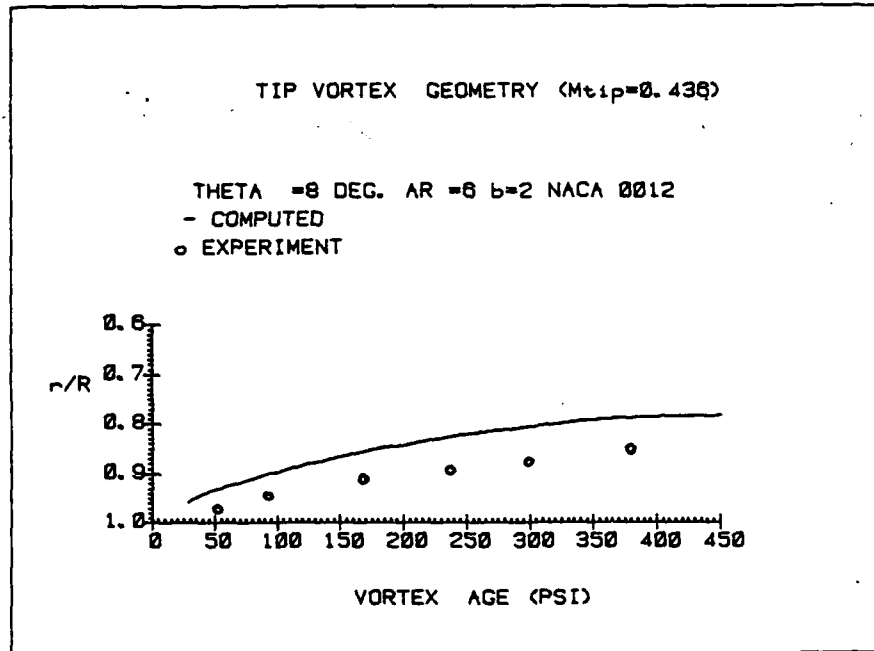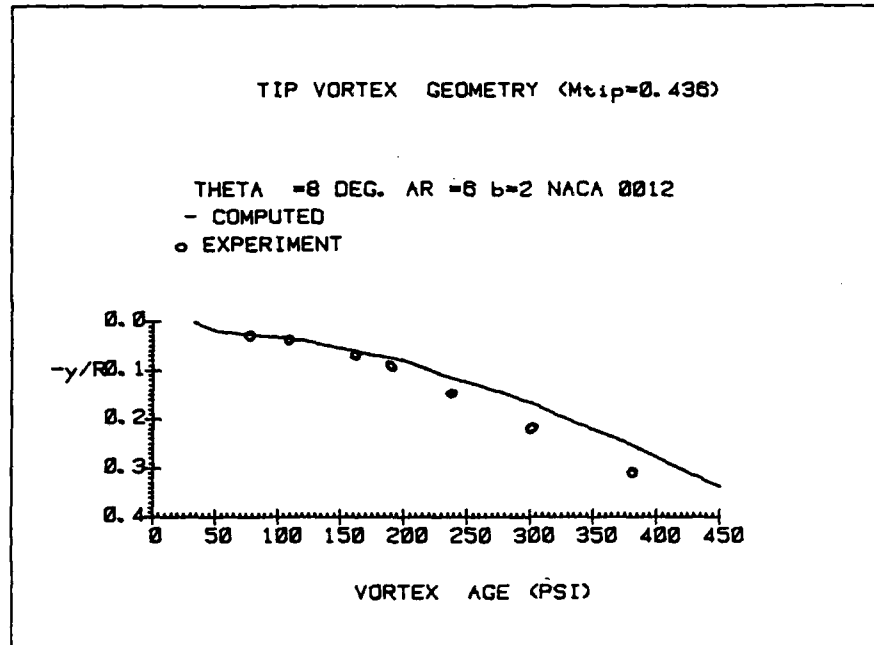o EXPERIMENT

r/R

VORTEX AGE (PSI)

Figure 20: Comparison of Tip Vortex Coordinates for Low Aspect Ratio Two-Bladed Rotor with a Collective Pitch of 8° and NACA0012 Profile at Subsonic Tip Speed with Experimental Data of Caradonna [34]
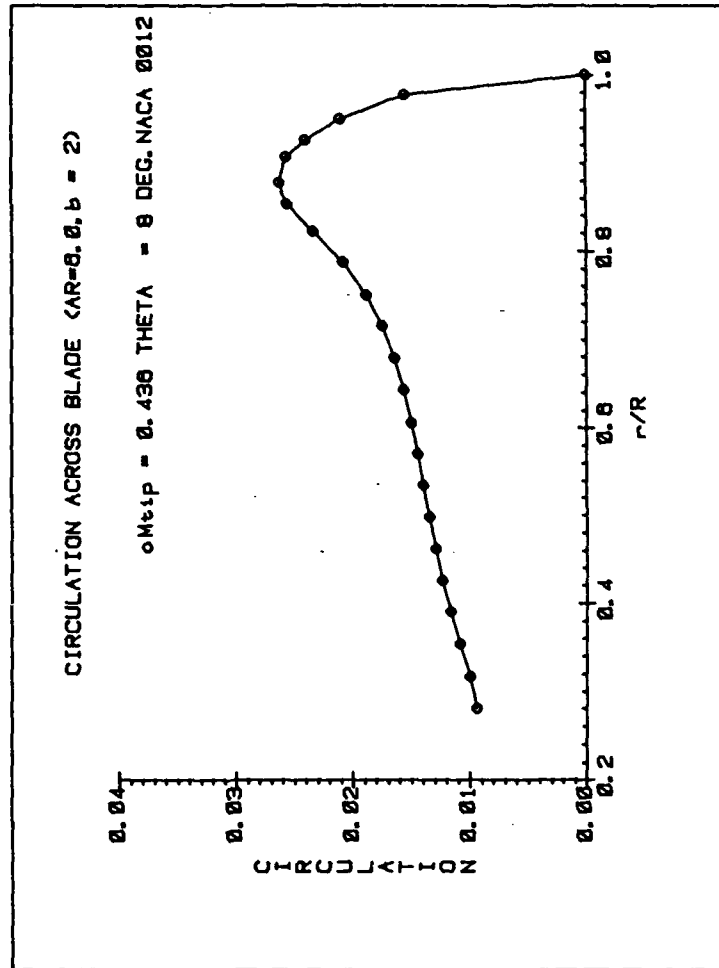
63

Figure 21: Blade Circulation Distribution for Low Aspect Ratio Two-Bladed Rotor with a Collective Pitch of 8° and NACA0012 Profile at Subsonic Tip Speed

surface pressure distributions for the 68% and 89% radial locations compare very well with experimentally measured data (Figure 22).

The computed solutions for transonic tip speed are presented in Figures 23 through Figure 25. The computed tip vortex axial coordinate and radial contraction are given in Figure 23. The bound circulation for this rotor is given in Figure 24. Chordwise surface pressure distributions compare favorably with the experimental data at all radial stations. Figure 25 illustrates the data correlation at the 68%, 80%, 89% and 96% radial locations. The calculated suction pressure, in regions near the region of tip vortex passage are accurately predicted for all but the last station which is very close to the tip. To resolve this region a finer grid is required there. From, Figure 22 and Figure 25 it is easily seen that inboard pressure distributions are only slightly affected by rotor speed. However, the outboard sections show considerable pressure alteration and shock development as the tip Mach number approaches sonic values.

4.2 Comparison of Results for Four-Blade Rotors

Even though good results were obtained with two-blade rotors, four-blade rotors present a crucial test for HELIX I since there the vortex from each blade passes much closer to the preceding blade. Also most modern rotors have four blades. As discussed above, the two-blade rotor results presented were done with an initial formulation of the vortex embedding method. Results for four-blade rotors were obtained using the new formulation described in Section 3.5.1. The first four-blade case computed involved blade number 7 of Reference [35]. The apsect ratio of this rotor is 15, with a $0A209$ profile and a collective pitch of 10^0. The blade has a linear twist such that the pitch is increased by 8.3^0 from root to

THETA =8 DEG. NACA 0012 ,Mtip=0.436
- COMPUTED
o EXPERIMENT UPPER SURFACE
x EXPERIMENT LOWER SURFACE

X/C
CHORDWISE PRESSURE DISTRIBUTION (AR =6, b =2, r/R=0.68)

THETA =8 DEG. NACA 0012 ,Mtip=0.436
- COMPUTED
o EXPERIMENT UPPER SURFACE
x EXPERIMENT LOWER SURFACE

X/C
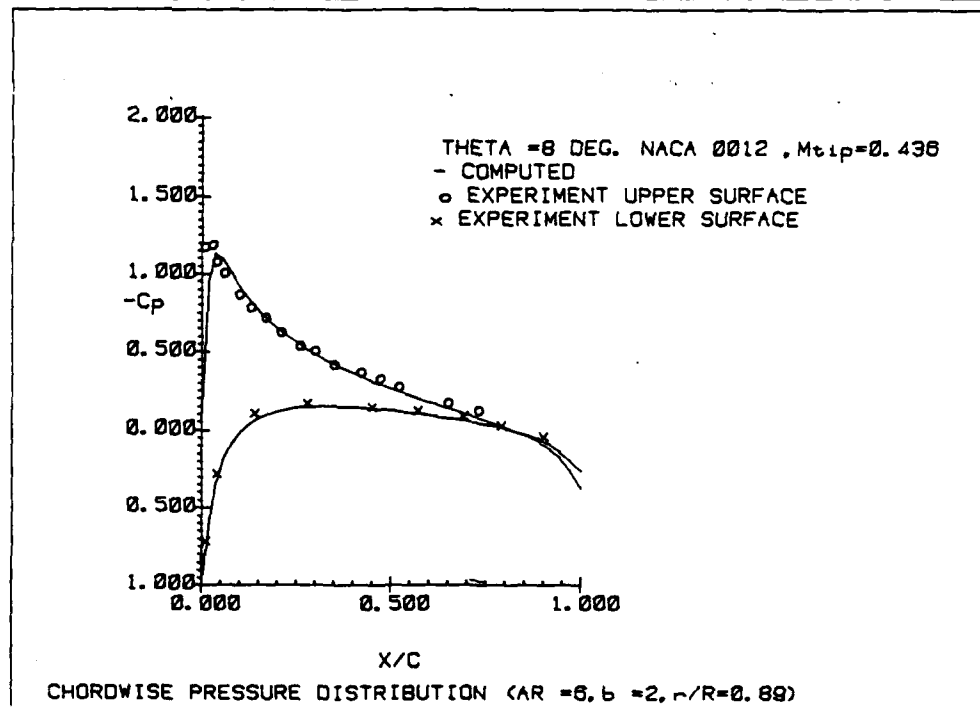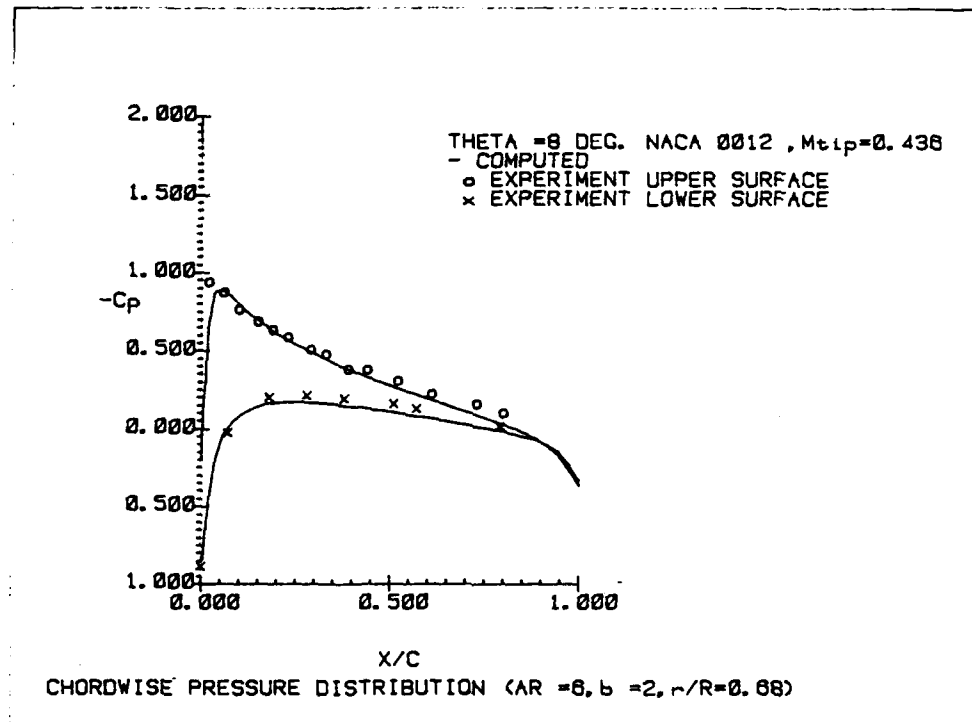CHORDWISE PRESSURE DISTRIBUTION (AR =6, b =2, r/R=0.89)

Figure 22: Comparison of Chordwise Pressure Distribution for Low Aspect
Ratio Two-Bladed Rotor with a Collective Pitch of 8^0, NACA0012
Profile at Subsonic Tip Speed with Experimental Data of
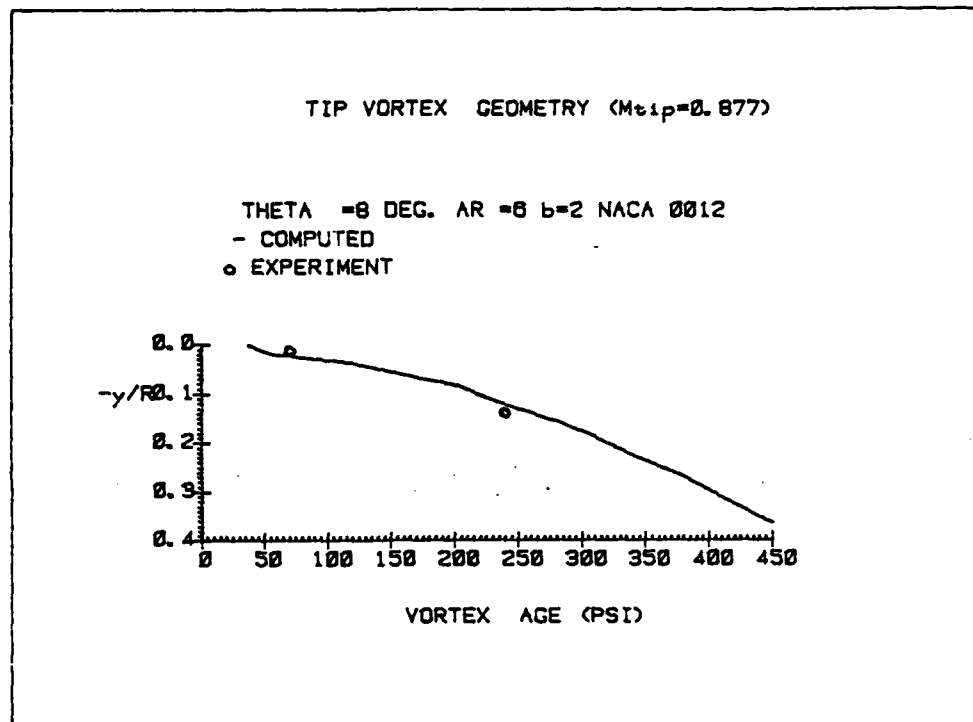Caradonna [34]

Figure 23: Comparison of Tip Vortex Coordinates for Low Aspect Ratio Two-Bladed Rotor with a Collective of 8^0 and NACA0012 Profile at Transonic Tip Speed with Experimental Data of Caradonna [34]
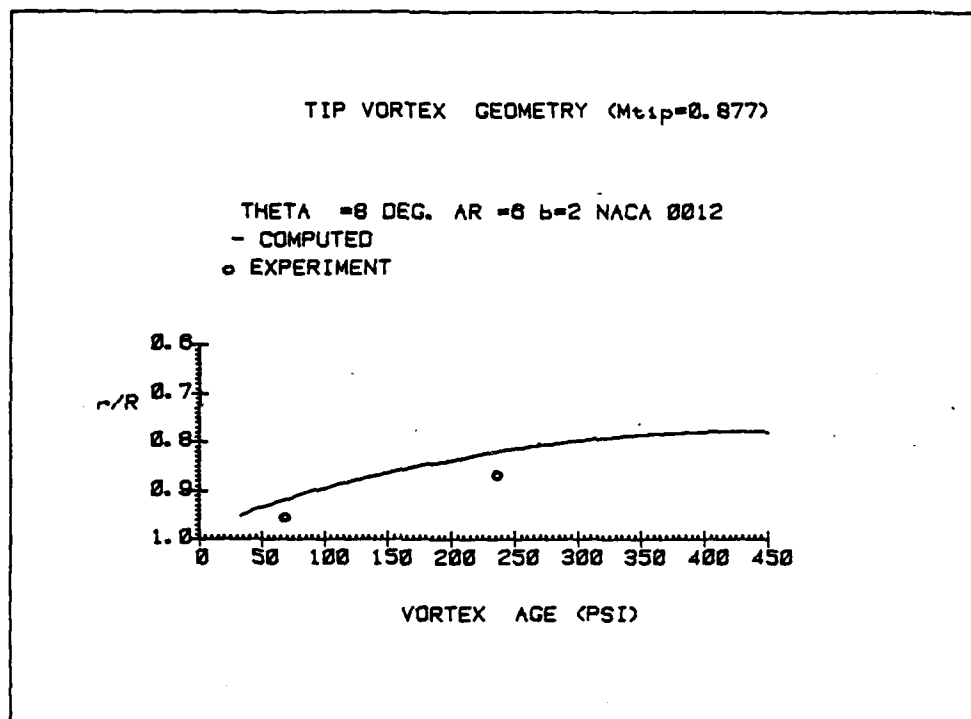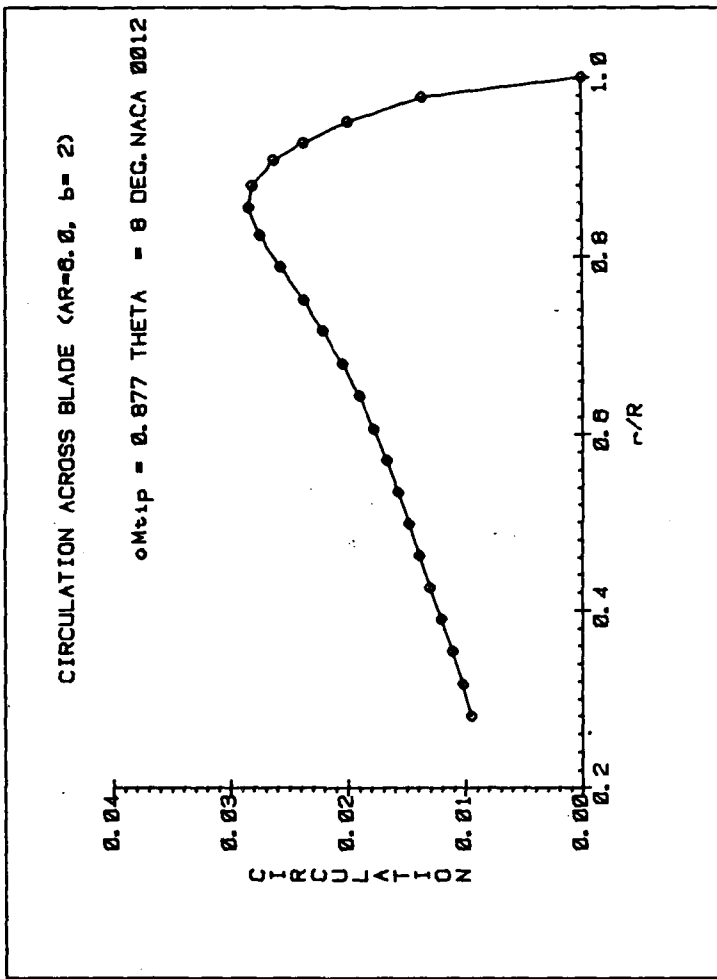
Figure 23: (continued)

Figure 24: Blade Circulation Distribution for Low Aspect Ratio Two-Bladed Rotor with a Collective Pitch of 8⁰ and NACA0012 Profile at Transonic Tip Speed

THETA =8 DEG. NACA 0012 ,Mtip=0.877
— COMPUTED
o EXPERIMENT UPPER SURFACE
x EXPERIMENT LOWER SURFACE

$-C_P$

X/C
CHORDWISE PRESSURE DISTRIBUTION (AR =8, b =2, r/R=0.80)

THETA =8 DEG. NACA 0012 ,Mtip=0.877
— COMPUTED
o EXPERIMENT UPPER SURFACE
x EXPERIMENT LOWER SURFACE

$-C_P$

X/C
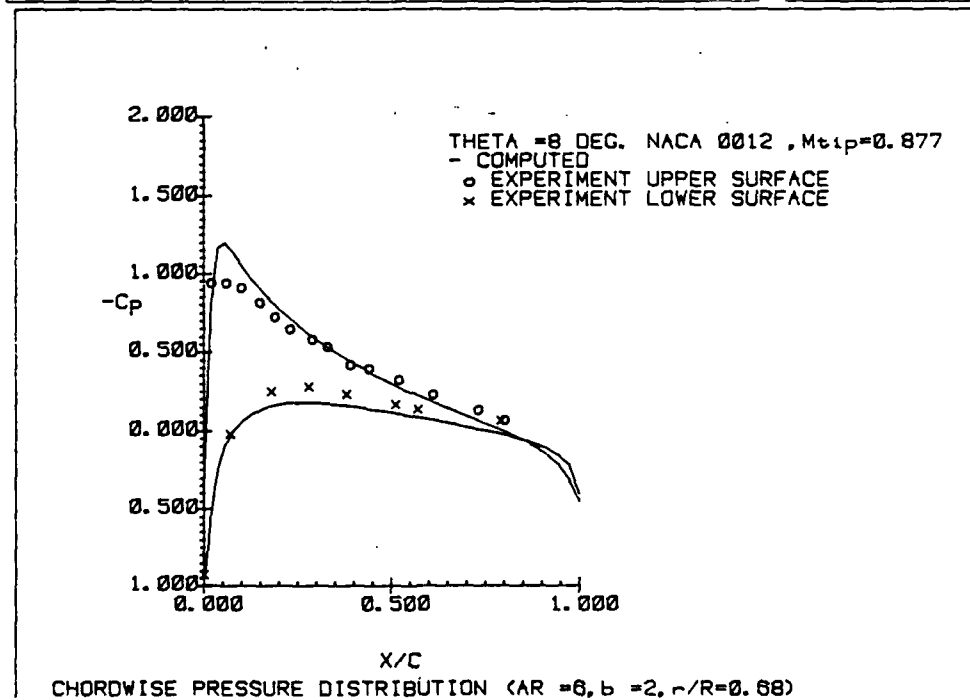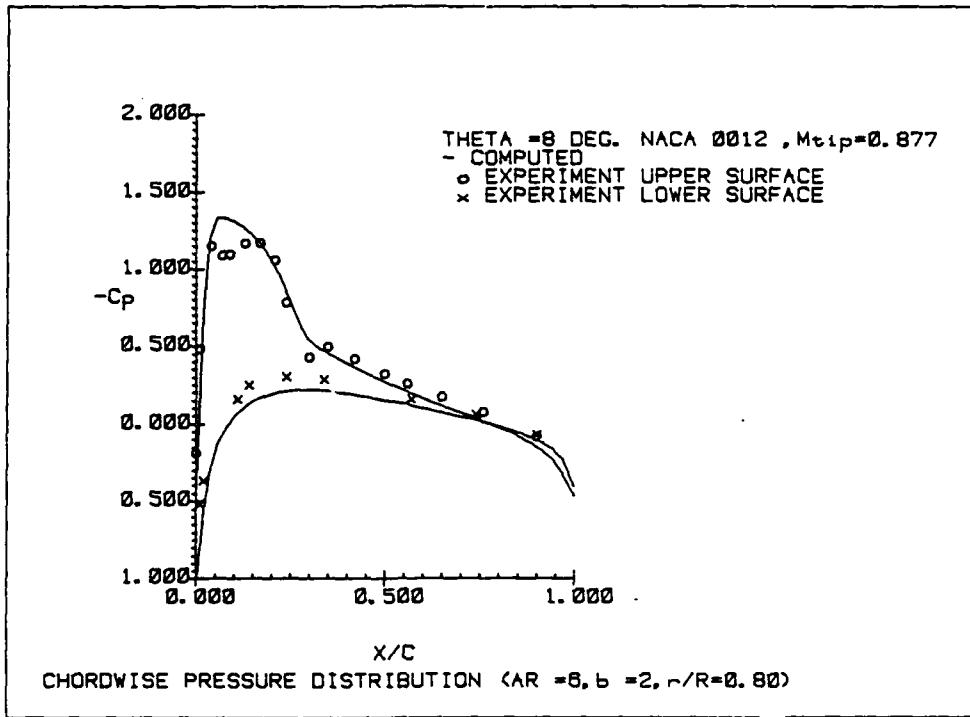CHORDWISE PRESSURE DISTRIBUTION (AR =8, b =2, r/R=0.68)

Figure 25: Comparison of Chordwise Pressure Distribution for Low Aspect
Ratio Two-Bladed Rotor with a Collective Pitch of 8^0, NACA0012
Profile at Transonic Tip Speed with Experimental Data of
Caradonna [34]

THETA =8 DEG. NACA 0012 , Mtip=0.877
- COMPUTED
 o EXPERIMENT UPPER SURFACE
 x EXPERIMENT LOWER SURFACE

2.000
1.500
1.000
-Cp
0.500
0.000
0.500
1.000

0.000   0.500   1.000

X/C
CHORDWISE PRESSURE DISTRIBUTION (AR =8, b =2, r/R=0.96)

THETA =8 DEG. NACA 0012 , Mtip=0.877
- COMPUTED
 o EXPERIMENT UPPER SURFACE
 x EXPERIMENT LOWER SURFACE

2.000
1.500
1.000
-Cp
0.500
0.000
0.500
1.000

0.000   0.500   1.000

X/C
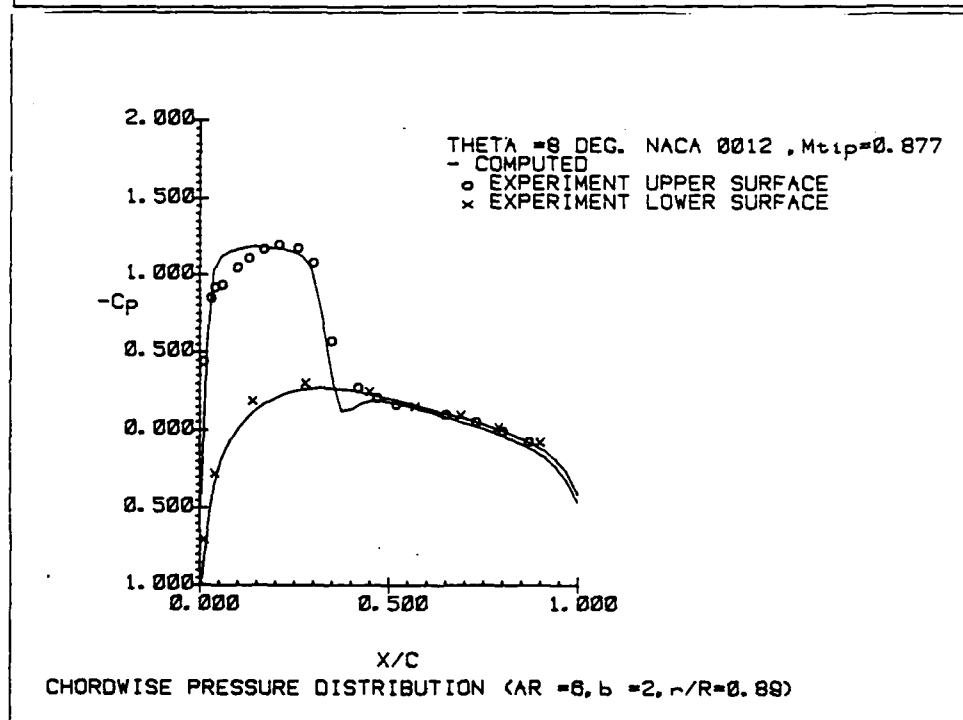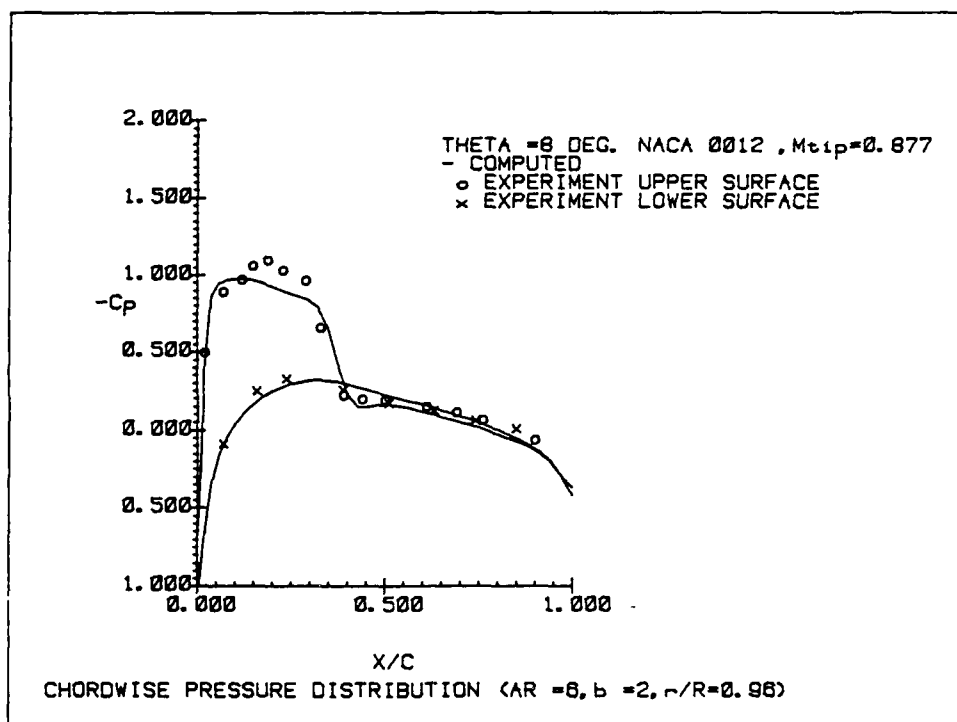CHORDWISE PRESSURE DISTRIBUTION (AR =8, b =2, r/R=0.89)

Figure 25: (continued)

tip. In Figure 26 the computed vortex geometry together with experimental data is presented. In Figure 27 the computed load distribution is plotted as a function of span and compared with experiment. Where experimental results are available agreement is similar to that obtained in the two-blade cases.

Finally a high aspect ratio $(AR = 18.2)$ four-blade rotor configuration with a NACA0012 profile, -8^0 linear twist and a collective pitch of 8^0 was analyzed. The experimental data used for comparison were obtained from Reference [4]. As the number of blades increase, each blade is closer to the tip vortex generated by the blade ahead due to the reduced separation between the blades. This causes an increased aerodynamic interference and a steep increase in load distribution near the tip region. This can be clearly seen in Figure 28, where the load distribution is presented as a function of normalized radial distance. The computed tip vortex axial and radial coordinates are presented in Figure 29. Agreement with experiment is seen to be good in this case.

4.3 General Features of the Solution and Wake Geometry

Several general features of the tip vortex geometry are evident in Figures 20 through 29. When an element of the tip vortex is shed from a blade, its axial rate of descent is low until it passes beneath the following blade. At that point, the tip vortex element lies radially inboard of the tip vortex of the following blade and thus experiences a large downward induced velocity. The axial tranport velocities before and after the passage of the following blade are fairly constant in the near wake, as can be seen from the substantially linear variations of the axial displacement, $\bar{y}_T$, with wake azimuth angle in these regions. The radial displacement, $\bar{r}_T$, of the tip vortex decays in approximately exponentially with increasing azimuth angle.

TIP VORTEX COORDINATES (AXIAL)

Mtip = 0.4, AR =15 b=4 OA209
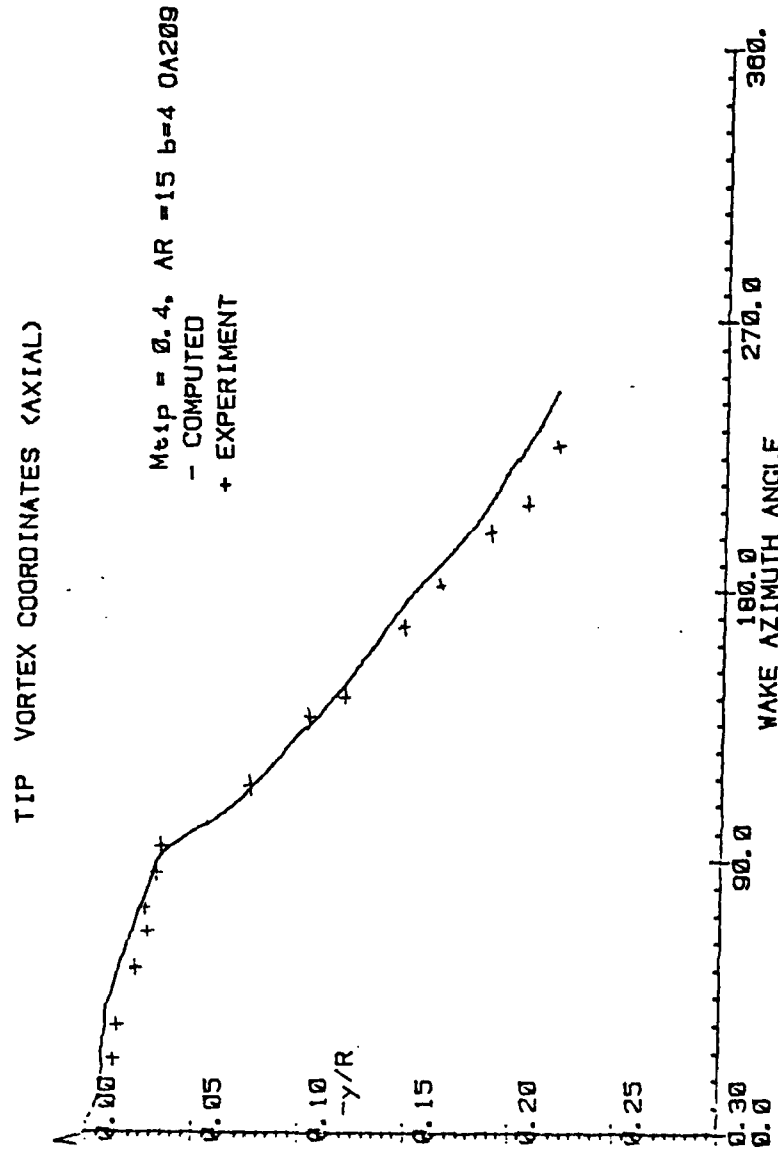— COMPUTED
+ EXPERIMENT

Figure 26: Comparison of Tip Vortex Coordinates for a Four-Bladed High Aspect Ratio Rotor with −8.3° Linear Twist and 10° Collective Pitch and OA209 Profile with Experimental Data of Maresca [35]

73

TIP VORTEX COORDINATES (RADIAL)

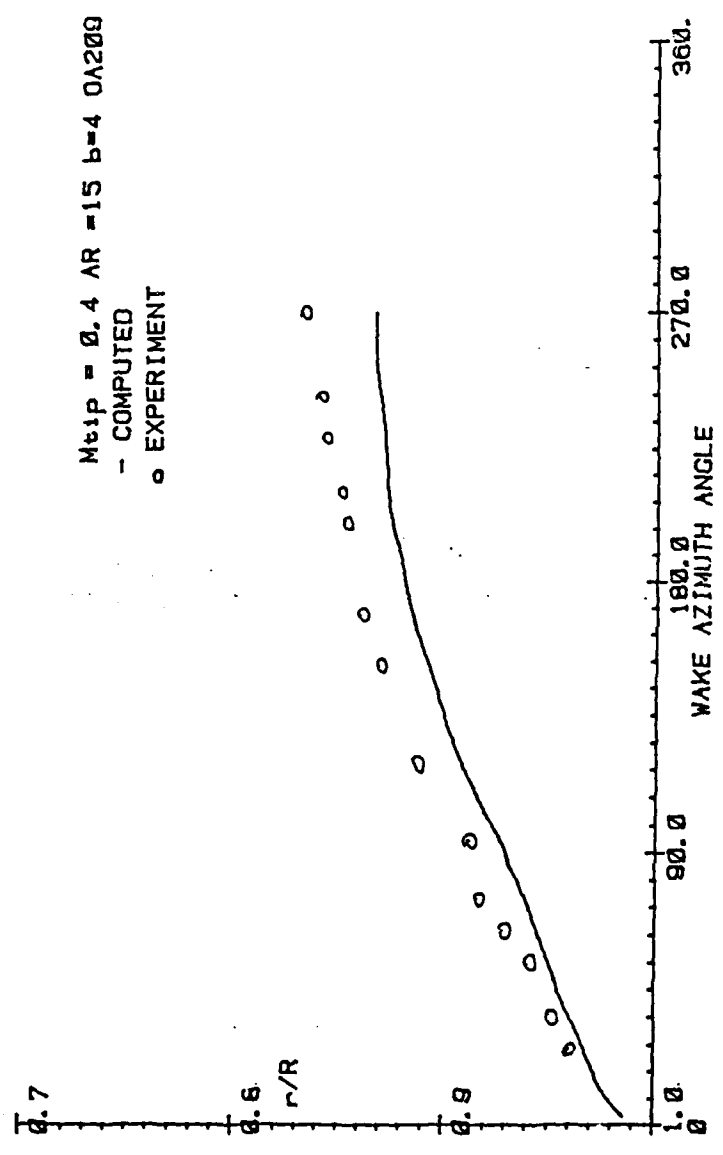Mtip = 0.4 AR =15 b=4 0A200

— COMPUTED
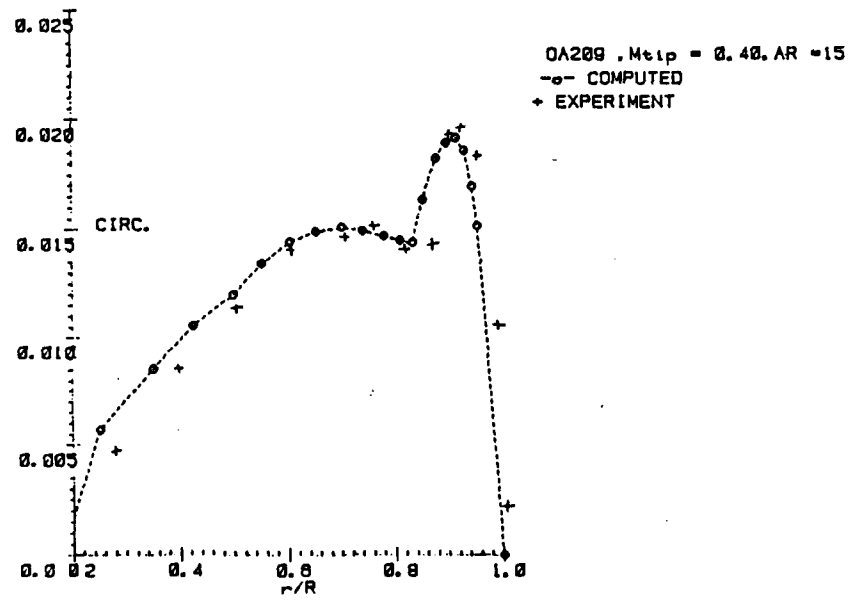o EXPERIMENT

Figure 26: (continued)

Figure 27: Comparison of Blade Circulation Distribution for a Four-Bladed High Aspect Ratio Rotor with $-8.3''$ Linear Twist and $10''$ Collective Pitch and OA209 Profile with Experimental Data of Maresca [35]

SPANWISE SECTION CIRCULATION (AR =18.2 b=4.

Figure 28: Blade Circulation Distribution for a Four-Bladed High Aspect Ratio -8^0 Rotor with Linear Twist and 8^0 Collective Pitch with NACA0012 Profile

TIP VORTEX COORDINATES (AXIAL)

Ntip = 0.48 b =4 NACA0012
Theta = -8.0 AR =18.2
- COMPUTED
-- EXPERIMENTAL FIT

WAKE AZIMUTH ANGLE

−γ/R

Figure 29: Comparison of Tip Vortex Coordinates for a Four-Bladed High
Aspect Ratio Rotor with -8^0 Linear Twist and 8^0 Collective Pitch with
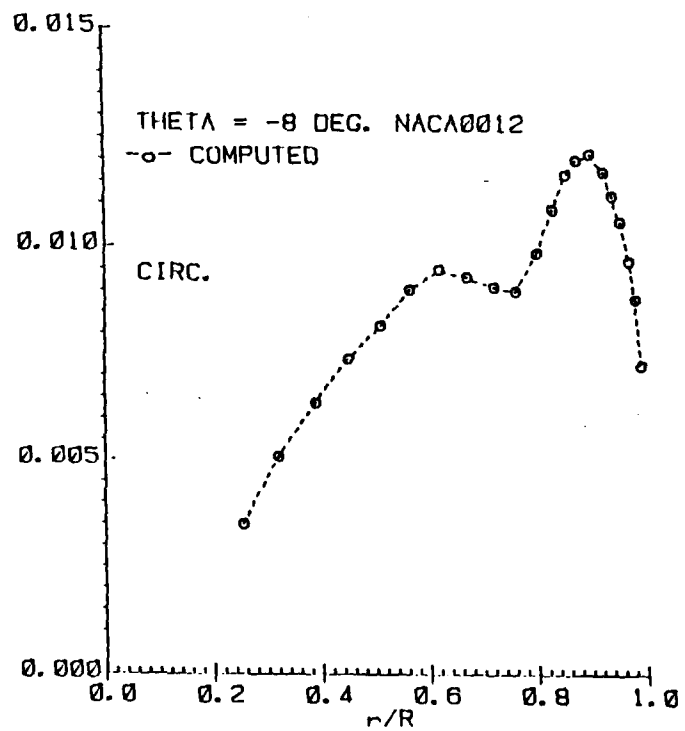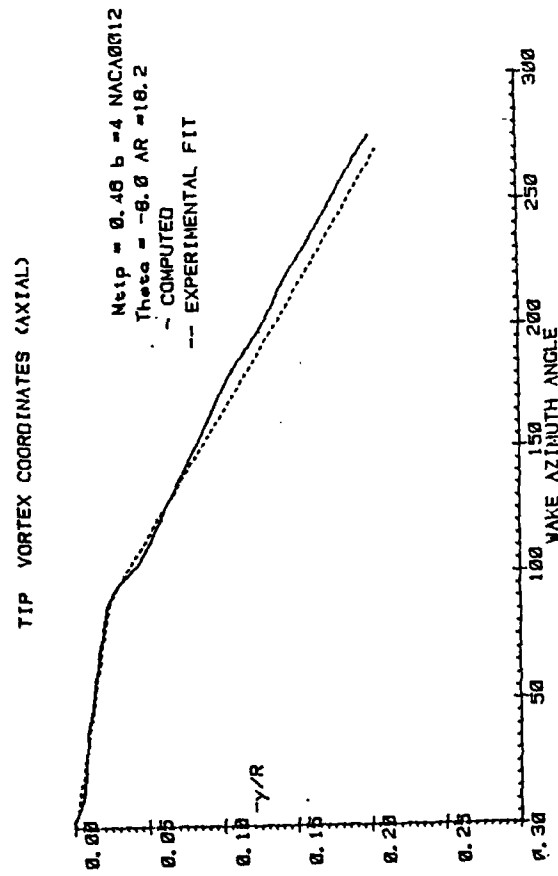NACA0012 Profile with Experimental Data of Landgrebe [4]

TIP VORTEX COORDINATES (radial)

Mtip = 0.48 b = 4 NACA0012
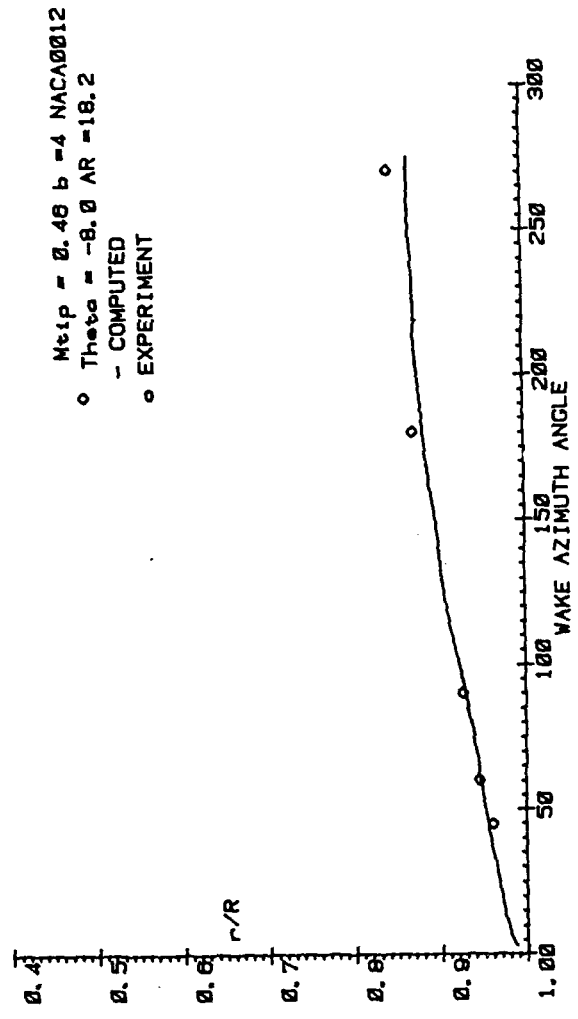Theta = -8.0 AR = 18.2
− COMPUTED
∘ EXPERIMENT

Figure 29: (continued)

The calculations presented were done using **HELIX I** on a 128 x 42 x 32 grid with 80 points on the airfoil and 18 span stations on the blade. Typical computation times on a VAX-11/785 system were about 5-6 minutes per iteration. The code has also been run on the NASA Ames Advanced Computational Facility's CRAY X-MP system. The CPU time for one iteration using this system is of the order of 10 secs. No special effort has yet been made to vectorize the program for use on this machine. Substantial improvements in the required computation time could be realized by restructuring the code to benefit fully from the CRAY vector processing capabilities. It is estimated that by doing this the execution time could be reduced by a factor of 3 to 4

Generally, a fully converged solution and a stable wake geometry are obtained in about 3 to 4 wake and vortical velocity updates, in between which an approximately converged potential solution is obtained. It is estimated that generation of one complete converged solution for loading and wake geometry takes about $1\frac{1}{2}$ hours of CPU time on the CRAY X-MP.

CHAPTER 5

CONCLUSIONS AND RECOMMENDATIONS

The main objectives of the research were to develop a comprehensive method for the prediction of hovering rotor performance in compressible flow. These have been met. The technique includes the all-important wake effect and allows for the analysis of advanced rotor configurations. As such, the constraints imposed by earlier techniques have been removed. Example calculations were presented which demonstrate the capabilities of the method including a stable calculation for the free wake flow. This has been demonstrated for both a traditional high aspect ratio blade and for an unconventional blade.

Results for the surface pressure distribution, the blade loading and the near wake geometry are all in good agreement with data but the far wake geometry should be the subject of a future study where improved calculations for $\bar{q}^v$ can be incorporated.

The basic algorithm has been demonstrated as complete in every respect except for the recommended refinement of selected components. In addition, the following are recommended:

1. Studies should be made for rotors with non-rectangular tip geometries to establish the significance of this geometry on the entire flow field calculation.

2. The extension to rotors in forward flight should be made. The major modification here is to the potential flow calculation which must then be based upon the unsteady flow equations.

BIBLIOGRAPHY

1. Landgrebe, A.J., "Overview of Helicopter Wake and Airloads Technology," Paper No. 18, Twelfth European Rotorcraft Forum, Garmisch-Partenkirchen, Federal Republic of Germany, September 1986.

2. Johnson, W., "Recent Developments in Rotary-Wing Aerodynamic Theory," AIAA Journal, Vol. 24, No. 8, August 1986.

3. Kocurek, J.D. and Tangler, J.L., "A Prescribed Wake Lifting Surface Hover Performance Analysis," Journal of the American Helicopter Society, Vol. 22, No. 1, January 1977.

4. Landgrebe, A.J., "An Analytical and Experimental Investigation of Helicopter Rotor Hover Performance and Wake Geometry Characteristics," USAAM-RDL TR-71-24, U.S. Army, June 1971.

5. Landgrebe, A.J., "An Analytical Method for Predicting Rotor Wake Geometry," Journal of the American Helicopter Society, Vol. 14, No. 4, October 1969.

6. Costes, J.J., "Application of Lifting Line Concept to Helicopter Computation," Paper Presented at European Rotorcraft and Powered Lift Aircraft Forum, September 1978.

7. Kocurek, J.D., "A Lifting Surface Performance Analysis with Circulation Coupled Wake for Advanced Configuration Hovering Rotors," Thesis (Ph.D.), Texas A & M University, College Station, May 1978.

8. Runyan, H.L., and Tai, H., "Lifting Surface Theory for a Helicopter Rotor in Forward Flight," NASA CR 169997, 1983.

9. Clark, D.R., et al., "Helicopter Flow Field Analysis," U.S. Army Research and Technology Laboratories, TR 79-4, April 1979.

10. Summa, J.M., and Maskew, B., "A Surface Singularity Method for Rotors in Hover or Climb," U.S. Army Aviation Research and Development Command, TR 81-D-23, December 1981.

11. Miller, R.H., "A Simplified Approach to the Free Wake Analysis of a Hovering Rotor," Vertica, Vol. 6, No. 2, 1982.

12. Murman, E.M., and Stremel, P.M., "A Vortex Wake Capturing Method Potential Flow Calculations," AIAA Paper 82-0947, June 1982.

13. Stremel, P.M., "Computational Methods for Non-Linear Vortex Wake Flowfields With Applications to Conventional and Rotating Wings," Thesis (M.S.), Massachusetts Institute of Technology, Cambridge, February 1982.

14. Roberts, T.W., "Computation of Potential Flows With Embedded Vortex Rings and Applications to Helicopter Rotor Wakes," Massachusetts Institute of Technology, Cambridge, CFDL-TR 83-5, September 1983.

15. Egolf, T.A., and Sparks, S.P., "Hovering Rotor Airload Prediction Using a Full Potential Analysis With Realistic Wake Geometry," Paper Presented at Annual National Forum of American Helicopter Society, May 1985.

16. Sankar, N.L., Wake, B.E., and Lekoudis, G.S., "Solution of Euler Equations for Fixed and Rotor Wing Configurations," AIAA Paper No. 81-1206, January 1985.

17. Strawn, R.C., and Caradonna, F.X., "Conservative Full-Potential Model for Unsteady Transonic Rotor Flows," AIAA Journal, Vol. 25, No. 2, February 1987.

18. Chang, I.C., and Tung, C., "Numerical Solution of the Full Potential Equation for Rotors and Oblique Wings Using a New Wake Model," AIAA Paper 85-0268, January 1985.

19. Johnson, Wayne, Helicopter Theory, Princeton University Press, 1980.

20. Clark, D.R., and Leiper, A.C., "The Free Wake Analysis, A Method for the Prediction of Helicopter Rotor Hovering Performance," Journal of the American Helicopter Society, Vol. 15, No. 1, January 1970.

21. Scully, M.P., "Computation of Helicopter Rotor Wake Geometry and Its Influence on Harmonic Loads," Massachusetts Institute of Technology, Cambridge, ASRL TR 178-1, March 1975.

22. Caradonna, F.X., and Isom, M.P., "Subsonic and Transonic Potential Flow Over Helicopter Rotor Blades," AIAA Journal, Vol. 10 No. 12 December 1972.

23. Steinhoff, J.S., Ramachandran, K., and Suryanarayana, K., "The Treatment of Convected Vortices in Compressible Potential Flow," AGARD Symposium on Aerodynamics of Vortical Type Flows in Three Dimensions," Rotterdam, Netherlands, April 1983.

24. Steinhoff, J.S., and Suryanarayana, K., "The Treatment of Vortex Sheets in Compressible Potential Flow," Proceedings, AIAA Symposium on Computational Fluid Dynamics, Danvers, July 1983.

25. Steinhoff, J.S., "Transonic Potential Flow Calculations," Unpublished Notes, UTSI, 1984.

26. Jameson, A., Caughey, D.A., "A Finite-Volume Method for Transonic Potential Flow Calculations," AIAA Paper No. 77-0406, June 1977.

27. Pelz, R., and Steinhoff, J.S., in Proceedings of the ASME Winter Meetings on Computers in Flow Predictions and Fluid Dynamics Experiments, Washington, D.C., 1981, p. 27.

28. Steinhoff, J.S., "Blending Method for Grid Generation," Journal of Computational Physics, Vol. 65, No. 2, August 1986.

29. Chow, R., et al., Grumman Research Memorandum RM-749, August 1982.

30. Jameson, A., "Iterative Solution of Transonic Flows Over Airfoils and Wings, Including Flows at Mach 1," Communications on Pure and Applied Mathematics, Vol. 27, 1974.

31. Ballhaus, W.F., Jameson, A., and Albert, J., "Implicit Approximate-Factorization Schemes for Steady Transonic Flow Problems," AIAA Journal, Vol. 16, No. 6, June 1978.

32. Steinhoff, J.S., and Ramachandran, K., "Free Wake Analysis of Compressible Rotor Flow Fields in Hover," Paper No. 20, Twelfth European Rotorcraft Forum, Garmisch-Partenkirchen, Federal Republic of Germany, September 1986.

33. Steinhoff, J.S., and Ramachandran, K., "Free Wake Analysis of Compressible Rotor Flows," AIAA Paper No. 87-0542, January 1987.

34. Caradonna, F.X., and Tung, C., "Experimental and Analytical Studies of a Model Helicopter Rotor in Hover," NASA TM-81232, September 1981.

35. Ramachandran, K., Steinhoff, J.S., and Tung, C., "Free Wake Analysis of Helicopter Rotor Blades in Hover by Finite Volume Technique," to be presented in the 43rd Annual Forum of the American Helicopter Society, St. Louis, MO, May 1987.